

1 **Phosphorylation alters FMRP granules and**
2 **determines their transport or protein synthesis abilities**
3

4
5 Shivani C. Kharod¹, Dongwoo Hwang², Heejun Choi⁴, Kyle J. Yoon², Pablo E. Castillo^{1,3} Robert
6 H. Singer^{1,2} and Young J. Yoon^{1,2,*}
7

8 ¹ *Dominick P. Purpura Department of Neuroscience, Albert Einstein College of Medicine, NY*
9 *10461*

10 ² *Department of Cell Biology, Albert Einstein College of Medicine, NY 10461*

11 ³ *Department of Psychiatry and Behavioral Sciences, Albert Einstein College of Medicine, NY*
12 *10461*

13 ⁴ *Janelia Research Campus, HHMI, Ashburn, VA 20147*
14

15
16
17
18
19 Running title: Phospho-state of FMRP changes granule structure and function
20

21
22 * Correspondence:
23

24 Young J. Yoon, Ph.D.
25 Dominick P. Purpura Department of Neuroscience
26 Albert Einstein College of Medicine
27 1300 Morris Park Avenue
28 Bronx, NY 10461
29 USA
30 Email: young.yoon@einsteinmed.edu
31

32
33
34 Figures: 5, Supplementary Figures: 6, Supplementary Movies: 14
35

36 Abstract: 138 words

37 Introduction: 420 words

38 Results: 2043 words

39 Discussion: 916 words

40 Methods: 2073 words

41 **Abstract**

42 Fragile X messenger ribonucleoprotein (FMRP) is an RNA-binding protein implicated in autism
43 that suppresses translation and forms granules. While FMRP function has been well-studied, how
44 phosphorylation regulates granule binding and function remains limited. Here, we found that
45 Fragile X patient-derived I304N mutant FMRP could not stably bind granules, underscoring the
46 essential nature of FMRP granule association for function. Next, phosphorylation on serine 499
47 (S499) led to differences in puncta size, intensity, contrast, and transport as shown by phospho-
48 deficient (S499A) and phospho-mimic (S499D) mutant FMRP granules. Additionally, S499D
49 exchanged slowly on granules relative to S499A, suggesting that phosphorylated FMRP can
50 attenuate translation. Furthermore, the S499A mutant enhanced translation in presynaptic
51 boutons of the mouse hippocampus. Thus, the phospho-state of FMRP altered the structure of
52 individual granules, leading to transport and translation to achieve spatiotemporal regulation of
53 local protein synthesis.

54 **KEYWORDS:** Fragile X messenger ribonucleoprotein (FMRP), granules, phosphorylation,
55 transport, translation, protein synthesis

56 Introduction

57 Fragile X messenger ribonucleoprotein (FMRP) is an RNA-binding protein implicated in mRNA
58 transport and protein synthesis¹⁻³. Loss of expression or loss-of-function mutations can lead to
59 intellectual disability with links to autism⁴. In *Fmr1* knock-out mice, the absence of FMRP led to
60 elevated protein production and altered synaptic plasticity^{5,6}. At the molecular level, studies have
61 shown that FMRP interacts with translating polyribosomes^{7,8} and mRNA^{9,10} to regulate protein
62 synthesis and travel along dendrites in an activity-dependent manner^{11,12}. In addition, recent
63 studies have elucidated different mechanisms of translational repression by FMRP through
64 interactions with the FMRP-interacting factor, CYFIP1¹³, stalled ribosomes¹⁰ and microRNA
65 complexes¹⁴. In mice, FMRP is phosphorylated on serine 499 (S499) which enhances its
66 association with polysomes and stalled ribosomes¹⁵. Subsequent studies reported that activation
67 of metabotropic glutamate receptors (mGluR) led to brief dephosphorylation of FMRP by protein
68 phosphatase 2A (PP2A)¹⁶ and facilitated the local translation of *Arc* mRNA in dendrites¹⁷. Also,
69 dephosphorylated FMRP gets ubiquitinated for degradation by the proteasome¹⁸. More recently,
70 we reported that FMRP phosphorylation plays a critical role in presynaptic structural and
71 functional plasticity¹⁹. Altogether, these studies point to phosphorylation of S499 as a critical
72 determinant in regulating FMRP function in translation.

73 One prominent feature of FMRP in neurons is the formation of Fragile X granules^{12,20-22}. FMRP is
74 a multivalent protein that can interact with mRNA, ribosomes, and other regulatory proteins for
75 transport and translational control in dendrites^{2,23}. FMRP can also bind with itself to mediate self-
76 assembly into relatively large intracellular structures in vitro^{24,25}. However, how changes in FMRP
77 granule structure are linked to changes in FMRP function in living cells remains unresolved. For
78 instance, it is unclear whether the Fragile X patient-derived I304N FMRP mutation, which has lost
79 the ability to bind ribosomes, can still form granules. More importantly, how phosphorylation and
80 dephosphorylation of FMRP can modify the structure of FMRP granules is unexplored. By
81 uncovering the features of FMRP granules that are translation-permissive or translation-
82 repressive, we can predict and assign the function of granules based on their structure and motion.

83 Here, we have investigated the granule-binding ability of GFP-FMRP, S499A, S499D, and I304N
84 to understand their impact on granule structure and function. Our findings suggest that
85 constitutively phosphorylated S499D mutant possesses greater processivity and long-distance
86 travel of FMRP granules by slowing translation. In contrast, S499A granules may favor scanning
87 through the dendrite through intermittent pauses to deliver newly synthesized proteins at

88 synapses. Thus, S499 phosphorylation is critical to changes in FMRP granule structure and may
89 function as a phospho-switch to regulate transport and local protein synthesis.

90

91 Results

92 ***Patient-derived I304N mutant FMRP does not stably bind FMRP granules***

93 A rare missense mutation on FMRP, I304N, was originally discovered in a Fragile X patient who
94 exhibited severe autistic behavior but expressed normal levels of FMRP mRNA and protein²⁶.
95 Sequencing the *Fmr1* locus revealed that the patient had a missense mutation within the KH2
96 domain of FMRP. Moreover, I304N mutant FMRP failed to co-fractionate with polyribosomes in
97 an I304N patient-derived cell line²⁷ and the I304N mouse model²⁸. We wanted to see if the loss
98 of polysome interaction could affect its ability to bind granules. When we expressed the I304N
99 FMRP (GFP-I304N) in neurons, we observed very few discrete puncta along with diffuse
100 fluorescence within dendrites (Fig. 1a). Continuous imaging of GFP-I304N in dendrites showed
101 no discernible granules over time in kymographs (Fig. 1b), indicating that either it was unable to
102 bind FMRP granules or that the bound population was obscured by the majority unbound
103 population. To achieve a higher resolution view of I304N FMRP movement, we conducted single
104 molecule tracking of individual FMRP proteins using HaloTag-I304N FMRP (Fig. 1c,d). HaloTag
105 uses self-labeling technology where bright, cell-permeable dyes conjugated to a HaloTag ligand
106 can covalently bind to the HaloTag, thereby rendering single molecules of Halo-FMRP visible by
107 fluorescence microscopy²⁹. We used deuterated JFX dyes³⁰, which have improved photostability
108 ideal for long-term single molecule imaging. When we compared the movement of individual Halo-
109 FMRP and Halo-I304N molecules, the trajectories for Halo-FMRP were either stationary or
110 followed a linear path (Fig. 1c and Supplemental Movie 1), suggesting that the moving FMRP
111 proteins were traveling along the cytoskeleton consistent with active transport. In contrast, most
112 Halo-I304N molecules appeared untethered with a large degree of freedom in their movement
113 (Fig. 1d and Supplemental Movie 1). On average, I304N FMRP proteins had higher median
114 displacement and velocity than Halo-FMRP (Fig. 1e,f). By plotting the particle intensity and size
115 we confirmed that no changes or loss of signal were observed during image acquisition due to
116 increased speed or photosensitivity (Fig. 1g,h). These results suggested that while I304N FMRP
117 had not completely lost affinity for molecular interactions, the binding time was so brief that the
118 unbound state prevailed where most proteins appeared to be freely diffusing. Notably, the lack of
119 stable granule-binding by the I304N FMRP would indicate that its interaction with ribosomes is
120 essential for FMRP granules, and loss of FMRP on granules is linked to FXS pathophysiology.

121 ***S499 phospho-mutant FMRP form distinct granules***

122 From activity-dependent dephosphorylation^{16,17} to hierarchical phosphorylation of neighboring
123 serine residues^{15,31}, S499 has been implicated as the major phospho-switch that governs FMRP

124 function^{23,32}. We reasoned that mutations on S499 that block or mimic phosphorylation would
125 allow us to capture intermediates of FMRP granules. We generated N-terminal GFP fusions to
126 wildtype and phospho-mutant FMRP¹⁵ driven by the human Synapsin promoter (Fig. 2a). FMRP
127 reporters were expressed in cultured hippocampal neurons at DIV7 for one week to assemble
128 with endogenous FMRP granules. As FMRP granules contain more than one FMRP²¹, reporter
129 expression results in exchange with FMRP in granules and becomes fluorescent over time (Fig.
130 2b,c). To confirm incorporation into FMRP granules, we performed immunofluorescence to GFP-
131 FMRP and endogenous FMRP in dendrites and observed colocalization (Fig. S1a). Moreover, co-
132 expression of GFP-FMRP with Halo-FMRP¹⁹ or ribosomal protein L10A fused to HaloTag showed
133 colocalization between FMRP with different tags and with ribosomes, respectively (Fig. S1b,c),
134 demonstrating that our FMRP reporters can assemble onto FMRP granules. As neurons are
135 sensitive to levels of FMRP³³, we limited the expression of our reporters to one week where we
136 could detect measurable differences in FMRP granules by fluorescence imaging and particle
137 analyses using TrackMate³⁴ on FIJI (Fig. 2d,e). Comparison of average dendritic expression of
138 GFP-FMRP and the phospho-mimic (S499D) mutant showed similar levels, whereas the
139 phospho-deficient (S499A) mutant expressed less as a result of degradation by the proteasome¹⁸
140 (Fig. S1d).

141 First, we characterized FMRP granules bound by our FMRP reporters to elucidate size, intensity,
142 and contrast as indicators of granule dimensions, amount of FMRP molecules present in granules,
143 and how well each reporter can cluster³⁵, respectively (Fig. 2f-h). The median diameter of GFP-
144 FMRP granules was around 0.5 μm , consistent with previous reports²¹. The fluorescence intensity
145 of GFP-FMRP granules exhibited a large distribution, suggesting that cycles of FMRP
146 phosphorylation and dephosphorylation can facilitate more FMRP molecules to incorporate into
147 individual granules. Notably, GFP-FMRP granules showed a range of contrast values
148 encompassing the phospho-mutants, suggesting a mixed population of granules with either
149 predominantly phosphorylated or dephosphorylated FMRP granules. The S499A mutant formed
150 granules that were relatively lower in size and intensity, suggesting that these granules were small
151 but tightly clustered (Fig. S2a). The higher contrast value can be attributed to S499A being
152 ubiquitinated and degraded leading to reduced overall dendritic levels¹⁸. Conversely, the S499D
153 mutant formed larger granules with slightly higher intensity and lower contrast than S499A,
154 indicating that S499D is bound diffusely on FMRP granules, giving a less compact appearance
155 (Fig. S2b). Since S499D mutant had been suggested to bind stalled polysomes preferentially¹⁵,
156 S499D-containing granules could be more disordered than a translating granule.

157 ***FMRP phospho-mutant reporters differ in processive movement***

158 As FMRP granules can travel throughout neurons^{11,36,37}, we next asked whether FMRP mutants
159 vary in their transport in dendrites. We acquired short continuous images (50 ms per frame for
160 400 frames) of dendrites expressing FMRP reporters (Fig. 3a) and used TrackMate (LAP tracker)
161 to analyze and classify moving particles (Fig. S3a-c and Supplemental Movies 2-4). Rather than
162 determine whether FMRP granules could move, we took a closer look to analyze and compare
163 the processive motion of granules in dendrites. Processivity of transport, or continuous activity of
164 molecular motors before detaching, is an important measure of how efficiently intracellular cargo
165 can travel in neurons to deliver molecules, such as mRNA, for local protein synthesis. In our
166 analysis, we defined processive motion as a particle that moves continuously along the same
167 direction for five or more consecutive frames, where each processive particle can be sorted by its
168 total displacement. We observed two populations of processive GFP-FMRP granules with high
169 and low displacements (Fig. 3b). The low displacement population was prominent in
170 dephosphorylated S499A granules, suggesting they tend to travel shorter distances with
171 intermittent pauses, consistent with scanning along the dendrite. On the other hand,
172 phosphorylated S499D granules showed a population with higher displacements indicative of
173 longer travel distances during each processive motion. These results suggest that phosphorylated
174 FMRP granules favor long-distance transport while dephosphorylated FMRP granules prefer
175 stop-and-go processive motion in search of a docking site.

176 ***FMRP exchange onto FMRP granules requires translation***

177 Given that FMRP phospho-mutants differ in their ability to associate with granules, this suggested
178 that FMRP granules were not static structures. We conducted fluorescence recovery after
179 photobleaching (FRAP) on individual FMRP granules to test whether unbound FMRP proteins
180 could exchange onto FMRP granules. We used low-power focused UV light to selectively
181 photobleach a single fluorescent FMRP puncta (Fig. 4a), reaching an average photobleaching
182 efficiency of 85%. As we did not detect rapid recovery within the first minute, we acquired longer
183 time-lapse images at 30-second intervals for 20 minutes. The FRAP assay was performed at
184 room temperature (22 °C) to minimize movement of the photobleached granule and to reduce the
185 likelihood of interference from other granules that actively traffic through dendrites at physiological
186 temperature.

187 Intriguingly, we observed a gradual and partial fluorescence recovery of GFP-FMRP (Fig. 4b,c
188 and Supplemental Movie 5). When the results were fit to a nonlinear regression curve, GFP-
189 FMRP reached half-maximal recovery after 2.5 minutes ($\tau = 172.5$ s) with an average recovery of

190 20% after 10 minutes (Fig. 3f, black circles). Also, the recovery plateaus after 10 minutes, which
191 suggested a steady-state exchange between inside and outside of the granule. In contrast,
192 G3BP1-GFP, a well-characterized granule protein^{38,39}, reached around 60% recovery after one
193 minute (Fig. S4a-c and Supplemental Movie 6). To test whether FMRP exchange depended on
194 translation, we performed FRAP in the presence of a translation elongation inhibitor,
195 cycloheximide (CHX), which would result in completely stalled ribosomes. In the presence of CHX,
196 GFP-FMRP granules exhibited a markedly reduced recovery (Fig. 4d,e and Supplemental Movie
197 7), suggesting that FMRP bound to CHX-stalled ribosomes do not exchange (Fig. 4f, red circles).
198 Comparison of recovery at the final timepoint showed a significant difference in fluorescence (Fig.
199 4g). Use of another translation elongation inhibitor, anisomycin, resulted in a similar reduction in
200 recovery (Fig. S4d-g and Supplemental Movie 8). Like GFP-FMRP, recovery of S499A topped
201 out at 20% (Figs. 4h,i, S5a,b and Supplemental Movies 9,10) with slightly faster kinetics ($\tau = 161.0$
202 s). However, in the presence of CHX, the initial recovery gradually decreased, suggesting that
203 S499A has a limited affinity for stalled ribosomes in granules. S499D fluorescence recovery was
204 the slowest ($\tau = 256.5$ s), eventually reaching 20% recovery after 20 minutes (Figs. 4j,k, S5c,d
205 and Supplemental Movies 11,12). The slow recovery is consistent with S499D binding to
206 attenuate translating ribosomes which reduced the recovery rate. Surprisingly, the initial recovery
207 kinetics of S499D was enhanced by CHX-treatment ($\tau = 30.8$ s). As CHX binds to the E-site of
208 the translating ribosome, the stable interaction between phosphorylated FMRP and ribosomes
209 may be occluded, leading to a faster exchange. Taken together, our data show that GFP-FMRP
210 on granules exchange at a timescale consistent with translation, and this exchange is sensitive
211 to translation inhibitors. Moreover, dephosphorylated FMRP preferentially bind translating
212 ribosomes and travel short distances, whereas phosphorylated FMRP exchanges slowly due to
213 attenuating translation while displacing larger distances (Fig. 4l).

214 Identifying the C-terminal portion of FMRP as a low-complexity region (LCR) was intriguing as it
215 hinted that FMRP granules may have functional consequences⁴⁰. As FMRP has multiple RNA-
216 binding domains, such as KH domains and RGG-box, along with the ability to bind ribosomes
217 through the KH2 domain, it was suggestive that FMRP may undergo phase separation⁴¹. We
218 generated a C-terminal truncation mutant, FMRP¹⁻⁴⁴⁴ (Δ C-term), which contained the Agenet and
219 KH1/2 domains and the nuclear export signal but not the S499 and the RGG box to test whether
220 it could bind to granules. When expressed in neurons, Δ C-term FMRP was able to bind granules,
221 albeit less clustered (Fig. S6a) as indicated by the large diameter, reduced intensity and contrast
222 like G3BP1 (Fig. S6b-e), which has been shown to phase separate⁴². These results support the

223 conclusion that S499 is necessary but not sufficient for tight granule binding. Fluorescence
224 recovery of Δ C-term FMRP granules was also similar to G3BP1 with fast recovery kinetics ($\tau =$
225 15.2 s), and CHX-treatment did not affect recovery (Fig. S6f-h and Supplemental Movies 13,14).
226 Conversely, when we expressed just the C-terminal portion of FMRP⁴²⁴⁻⁶¹⁴ (FMRP C-term), we
227 did not detect granules or localization to any discrete subcellular structure (Fig. S6i). While our
228 results suggest that the C-terminal region of FMRP may not independently form granules, there
229 could be FMRP-interactors on disparate regions of FMRP that may facilitate phase separation^{43,44}.

230 ***Phospho-deficient FMRP enhances local translation in mossy fiber boutons***

231 Recently, we have shown that presynaptic boutons can perform increased local protein synthesis
232 in response to presynaptic activity in an FMRP-dependent manner^{19,45}. Presynaptic
233 compartments such as hippocampal mossy fiber boutons provide an ideal subcellular
234 compartment to observe discrete, measurable differences in protein synthesis. To determine
235 whether the phospho-state of FMRP can change the translational output in presynaptic boutons,
236 we injected lentiviruses encoding Halo-FMRP or Halo-S499A into the dentate gyrus region of the
237 mouse hippocampus to target dentate granule cells, which give rise to mossy fibers. Following
238 the expression of these constructs, acute hippocampal slices were fluorescently labeled, and
239 mossy fiber boutons were imaged (Fig. 5a-c). Consistent with our findings in cultured neurons,
240 we found that the S499A mutant formed granules that were smaller, less bright, and more
241 compact when compared to Halo-FMRP (Fig. 5d-f). Next, to determine whether the difference in
242 granule clustering led to causal changes in protein synthesis, we used puromycin (PMY)
243 incorporation onto nascent peptides⁴⁶ to measure the total output of protein synthesis in the mossy
244 fiber tract (Fig. 5g,h). Using FMRP fluorescence as a mask, we quantified the average intensity
245 of the colocalized puromycin label and found that S499A granules correlated with an increase in
246 protein synthesis when compared to Halo-FMRP (Fig. 5i). Our results demonstrate that regulation
247 of FMRP granule structure and protein synthesis in mossy fiber boutons correlates with the
248 phosphorylation state of FMRP.

249 Discussion

250 In this study, we set out to better understand FMRP granule structure and function. Using FMRP
251 reporters and high resolution imaging in neurons harboring endogenous FMRP granules helped
252 identify distinguishing features that differ in mutant FMRP. For instance, our observation that the
253 FXS patient-derived I304N mutation could not form discrete granules suggests a possible linkage
254 to FXS. The integrity and maintenance of FMRP on granules could be an important factor in
255 neuronal function and physiology.

256 To capture FMRP granule intermediates, we focused on the well-characterized phospho-switch
257 S499 of FMRP. The current model of FMRP function is that phosphorylation on S499 results in a
258 translation-repressive state, and dephosphorylation leads to a translation-permissive state, where
259 FMRP likely mimics the phosphorylated state in neurons¹⁵. Upon mGluR activation, FMRP is
260 transiently dephosphorylated, thereby providing a temporal window of protein synthesis in an
261 activity-dependent manner. Using our FMRP phospho-mutant reporters, we could distinguish
262 differences in FMRP granules that were translation-permissive or -repressive (Figs. 2,3).
263 Regarding granule size and contrast, our observations were consistent with our expectations,
264 where the S499A mutant bound smaller and more discrete granules, while the S499D mutant
265 bound larger and less discrete granules relative to GFP-FMRP, reflecting their differing affinities
266 for granules. However, when we looked at the fluorescence intensity of GFP-FMRP granules, on
267 average, they were much brighter than either mutant. By blocking S499 from phosphorylation and
268 subsequent phosphorylation of neighboring serines^{15,31}, the phospho-mutant FMRP could not be
269 incorporated into granules in numbers comparable to GFP-FMRP. This observation suggests that
270 phosphorylation and dephosphorylation cycles on S499 can promote phosphorylation of
271 neighboring serines such that more GFP-FMRP can bind or assemble onto granules.

272 Given the differences in granules, we reasoned that the interaction of our FMRP reporters with
273 granules was not a static process. Our FRAP results for GFP-FMRP showed a partial recovery
274 that was blocked by the translation elongation inhibitor, CHX. The observation that GFP-FMRP
275 could exchange on granules through translating ribosomes was inconsistent with the model that
276 FMRP functions predominantly to stall ribosomes. However, it is conceivable that FMRP may be
277 tuning translation to enhance the fidelity of local protein synthesis. For instance, a previous report
278 showed that FMRP binds to its target mRNA along the coding sequence¹⁰, suggesting that FMRP-
279 binding was not sequence-specific within the open reading frames of target transcripts. The
280 results do not exclude the possibility that FMRP interaction with the coding regions of mRNA could

281 occur on attenuated or stalled ribosomes. Second, our β -actin translation reporter (which is not
282 an FMRP target) displayed a half-maximal recovery time of around 75 seconds in dendrites⁴⁷,
283 compared to >150 seconds with our GFP-FMRP reporters (Fig. 4), suggesting that FMRP-binding
284 may be slowing translation. Third, the observation that FMRP occupancy on mRNA can stabilize
285 target transcripts through codon optimization⁴⁸ will likely require active translation to protect FMRP
286 targets from mRNA surveillance and decay mechanisms⁴⁹. Taken together, there is a possibility
287 that FMRP may enhance the fidelity of local protein synthesis through attenuation of translation
288 rates rather than completely stalling translation.

289 Unexpectedly, S499D mutant exhibited an ability to exchange with CHX-stalled FMRP granules
290 (Fig. 4j). This result was surprising as phosphorylated FMRP should preferentially remain bound
291 to stalled ribosomes. The initial rapid recovery or exchange indicated less stable binding to
292 granules due to CHX-induced stalling. One explanation could be that FMRP may prefer to stall
293 translation at a specific elongation step of protein synthesis that “locks-in” FMRP onto granules,
294 and stalling ribosomes with CHX can lead to changes in ribosome conformation, thereby
295 destabilizing this interaction. The cryo-EM structure of the fly ribosome bound to dFMRP
296 suggested that KH1 and KH2 domains interact near the peptidyl site (P site) of the 80S ribosome⁵⁰.
297 Structural evidence that CHX binds to the tRNA exit site (E site) to block ribosome translocation
298 may force the P site to remain fully occupied and unable to ratchet^{51,52}. The growing nascent
299 peptide bound to tRNA in the P site and CHX bound to the E site may occlude stable interaction
300 between S499D FMRP and the ribosome.

301 The recovery levels observed in our FRAP assay was consistently around $20 \pm 10\%$ for FMRP
302 reporters (Fig. 4). Although we have shown that the recovery was translation-dependent, a large
303 population of FMRP did not recover, and their binding was translation-independent. The source
304 of this unrecoverable population could be attributed to FMRP bound to the untranslated regions
305 (UTRs) of mRNA. While there are differing opinions on whether FMRP can preferentially bind
306 RNA in the coding sequence or the guanine-rich G-quadruplex structures on the 3'UTR^{10,53}, our
307 results may indicate the presence of both interactions. Moreover, if FMRP bound to CYFIP1¹³ or
308 microRNA complexes¹⁴ are present, a significant population of FMRP with longer binding-times
309 may not recover in 20 minutes.

310 As FMRP is a negative translation regulator, our results support a clear partition of function for
311 phosphorylation and dephosphorylation. Although FMRP-induced translation stalling has been
312 simplified as an all-or-none event, it is likely that FMRP functions somewhere in between working

313 in conjunction with other factors to regulate protein synthesis, such as mRNA stability through
314 codon optimality⁴⁸, nonsense-mediated decay (NMD)⁵⁴ or m6A-mediated decay⁵⁵, all of which
315 may not directly lead to or require completely stalled ribosomes. Moreover, it will be interesting to
316 directly compare the translation rates of FMRP and non-FMRP target mRNAs to determine
317 whether FMRP preferentially stalls or slows translation. In sum, our report demonstrates that
318 FMRP granules are dynamic structures, and elucidating how FMRP asserts control of transport
319 and local protein synthesis may benefit from high resolution studies.

320 **Methods**

321 **Animals**

322 Experimental procedures adhered to NIH and Albert Einstein College of Medicine Institutional
323 Animal Care and Use Committee guidelines. Mice were group-housed in a standard 12 hr light/12
324 hr dark cycle. Dissociated mouse hippocampal neuron culture and acute transverse slices were
325 prepared from male and female mice (P1 and P21-45, respectively): C57BL/6J (Charles River).
326 Plasmids used in this work are available on Addgene. Detailed protocols and reagent information
327 herein are available upon request.

328 **Plasmids and lentivirus production**

329 Lentiviral expression vectors for GFP fused to FMRP, S499A and S499D were prepared by
330 restriction digest cloning using PCR amplification of EGFP-FMRP sequence from p-EGFP-C1-
331 Flag-mFmr1(wt), p-EGFP-C1-Flag-mFmr1(A) or p-EGFP-C1-Flag-mFmr1(D), respectively. The
332 EGFP-FMRP, S499A and S499D plasmids were a gift from Stephanie Ceman (Addgene plasmids
333 #87929, #87913 and #87914). HaloTag versions of FMRP reporters were generated by replacing
334 GFP with HaloTag. The I304N mutant FMRP was generated using Q5 Site-Directed Mutagenesis
335 Kit (NEB). G3BP1-GFP plasmid was a gift from Jeff Chao (Addgene plasmid #119950). Lentiviral
336 particles were generated by transfecting ENV (pMD2.VSVG), packaging (pMDLg/pRRE), REV
337 (pRSV-Rev) along with the expression vector into HEK293T cells using calcium phosphate. Viral
338 supernatant was concentrated using Lenti-X concentrator (Takara Bio) according to
339 manufacturer's instruction. Virus particles were resuspended in Neurobasal A (Invitrogen) and
340 stored at -80 °C. High-titer lentivirus were produced in the Einstein Genetic Engineering and Gene
341 Therapy core according to standard protocol. Titer was quantified using fluorescence, RT-PCR
342 and ELISA.

343 **Dissociated mouse hippocampal neuron culture**

344 Post-natal day 1 (P1) mouse hippocampal tissue was isolated from C57BL/6 wildtype newborn
345 pups. Hippocampi were dissociated in 0.25% trypsin, triturated and plated onto poly-D-lysine
346 (Sigma) coated glass-bottomed dishes (MatTek) at 35,000-50,000 cells per dish. Neurons were
347 cultured in Neurobasal A supplemented with B-27 (Invitrogen) and GlutaMAX (Invitrogen).

348 **Slice preparation**

349 Acute transverse slices were prepared as follows: briefly, mice were decapitated, and brains were
350 removed quickly and put into ice cold sucrose cutting solution or NMDG cutting solution. The
351 sucrose cutting solution contained (in mM): 215 sucrose, 20 glucose, 26 NaHCO₃, 4 MgCl₂, 4

352 MgSO₄, 1.6 NaH₂PO₄, 2.5 KCl, and 1 CaCl₂. The NMDG cutting solution contained (in mM): 93
353 N-Methyl-d-glucamin, 2.5 KCl, 1.25 NaH₂PO₄, 30 NaHCO₃, 20 HEPES, 25 D-glucose, 2 Thiourea,
354 5 Na-Ascorbate, 3 Na-Pyruvate, 0.5 CaCl₂, 10 MgCl₂. Mice over P35 were cut in NMDG. The
355 hippocampi were isolated and cut using a VT1200S vibratome (Leica) at a thickness of 300 µm.
356 The slices were then transferred to 32 °C ACSF for 30 minutes and then kept at room temperature
357 (RT) for at least 1 hr before recording. For P21 mice: After ice-cold cutting, the slices recovered
358 at RT (in 50% sucrose, 50% ACSF) for < 30 minutes and then at RT for 1 hr in ACSF. The artificial
359 cerebrospinal fluid (ACSF) recording solution contained (in mM): 124 NaCl, 26 NaHCO₃, 10
360 glucose, 2.5 KCl, 1 NaH₂PO₄, 2.5 CaCl₂, and 1.3 MgSO₄. All solutions were bubbled with 95% O₂
361 and 5% CO₂ for at least 30 minutes. All experiments in acute slices were performed at 25.5 ±
362 0.1 °C.

363 **Sample preparation and live imaging**

364 Cultured hippocampal neurons were infected with lentivirus at DIV7 and imaged after 3 days at
365 DIV10 or after one week at DIV14, unless noted otherwise. Prior to imaging, the neurobasal media
366 was exchanged to Hibernate A low fluorescence (BrainBits) and allowed to equilibrate for 30
367 minutes at 37 °C prior to imaging at 22 °C. Cycloheximide (CHX, Sigma) 100 µg/ml or anisomycin
368 (50 µM, Sigma) were introduced into the media after equilibration and allowed to incubate an
369 additional 30 minutes at 37 °C prior to imaging at 22 °C. For HaloTag labeling, cells were treated
370 with 10 nM JF549HTL or JF646HTL (Promega) for 15 minutes, followed by 3x washes and
371 incubation in Hibernate A (low fluorescence) for at least one hour. Cells were washed again in
372 Hibernate A prior to imaging at 35 °C. For single molecule imaging, 10 nM JFX549 and 10 nM
373 JFX646 were mixed at 20:1 ratio and added to neuron cultures and labeled for 15 minutes and
374 washed as above. The deuterated JFX Janelia Fluors were kindly provided by Dr. Luke Lavis at
375 the Janelia Research Campus.

376 **Stereotaxic injections**

377 WT C57BL/6J mice were stereotactically injected with high titer Halo-FMRP or Halo-S499A
378 lentivirus into the dentate gyrus region between P21-P24 using established coordinates (-2.2
379 posterior to Bregma, 2.0 laterally, and 2.0 ventral from dura) using a total volume of 1.5
380 µL/hemisphere at a flow rate of 0.2 µL/min. After 2-3 weeks of recovery, mice were humanely
381 killed and acute hippocampal slices were prepared as described above. For labeling Halo-FMRP,
382 cell-permeable Halo-ligand was bath-applied. Slices were labeled with JF549-HTL (100 nM) in
383 ACSF in a chamber oxygenated with 95%O₂/5% CO₂ for 1 hour. Slices were fixed with 4% PFA
384 and mounted using ProLong Diamond (Invitrogen).

385 **Immunofluorescence**

386 For immunofluorescence, neurons were fixed in 4% paraformaldehyde solution (PFA) and
387 permeabilized. After blocking in normal goat serum, cells were treated with primary antibodies:
388 anti-GFP (Aves lab) or anti-FMRP (Abcam; ab17722), followed by secondary antibodies: Goat
389 anti-chicken Alexa Fluor 647 (ThermoFisher) or goat anti-rabbit Cy3 (Sigma) and DAPI. For
390 hippocampal tissue, acute slices were washed twice in 1x PBS then incubated in blocking buffer
391 (4% goat serum in 1x PBS + 2% BSA + 0.1% Tx-100) for 1 hr at RT. Primary antibodies were
392 diluted directly into the antibody buffer (blocking buffer without goat serum) and floating slices
393 were incubated overnight at 4 °C. After 4 washes with 1x PBS, slices were incubated in secondary
394 antibodies (Invitrogen) diluted in blocking buffer overnight at 4 °C. Slices were washed 5x with 1x
395 PBS, then mounted using ProLong Diamond (Invitrogen).

396 **Puromycylation**

397 Acute slices were cut (as described in Slice preparation) 3 weeks after stereotaxic injection and
398 checked for expression using an epifluorescence microscope. Slices were incubated with
399 puromycin (50 µM, Sigma) for 30 minutes. Slices were then fixed for 1 hr in 4% PFA, blocked for
400 30 minutes, and stained according to the immunohistochemistry protocol above (primary
401 antibodies: anti-ZnT3, rabbit polyclonal, 1:500, Synaptic Systems; anti-puromycin 1:1000, EMD
402 Millipore) and imaged on the Zeiss LSM 880 with Airyscan using a LD LCI Plan-Apochromat
403 25x/0.8 mm Korr DIC M27 and 1.8x zoom. Images were Airyscan processed prior to analysis.
404 Quantification was performed using FIJI by drawing regions of interest in the ZnT3 channel in
405 which puromycin fluorescence intensity was measured in stratum lucidum. For stratum radiatum
406 control, puromycin signal in regions of interest distal to the stratum lucidum as indicated by the
407 ZnT3 labeling were measured.

408 **Fluorescence microscopy**

409 Acquisition of fluorescence images were performed on a wide field microscope previously
410 described⁵⁶. In brief, the inverted widefield microscope was equipped with 491 nm (Cobolt), 561
411 nm (Lasertechnik) and 640 nm (Coherent) laser lines along with a UApo 150x 1.45 NA or PlanApo
412 60x 1.45 NA oil immersion objectives (Olympus). Images were acquired on an EMCCD camera
413 (Andor). Images were 512x512 in size with a pixel size of 106.7 nm (150x) or 266.7 nm (60x).
414 Streaming videos of FMRP granules in dendrites were acquired by continuous imaging at 50 ms
415 intervals for 400 or more frames from a single z-plane. All z-series images (0.2 µm steps) were
416 maximum projected prior to analysis. For photobleaching fluorescent granules, we used the 405
417 nm UV laser (Omikron) along with a motorized focus lens (Thorlabs) which delivers focused light

418 to a diffraction limited spot. After acquiring a pre-image, fluorescent granules were exposed to UV
419 light at 10% power for 5 seconds for photobleaching. Typically, our photobleaching resulted in
420 greater than 85% average photobleaching efficiency. Time-lapse z-series stacks (21 steps at 0.2
421 μm per step) were acquired for both 491 nm (GFP) and 561 nm (mCherry) channels every 30
422 seconds for 41 time-points (20 minutes). The cells were maintained at 22 °C throughout imaging
423 through a humidified stage top incubator (Tokai Hit). For single molecule imaging of sparsely
424 labeled Halo-FMRP or Halo-I304N, we first identified neurons labeled with JFX549 and switched
425 to image JFX646. We acquired streaming images at 50 ms intervals for 1000 images (50 seconds)
426 using 640 nm laser at high power (50%). We used the first 100 images for particle detection and
427 tracking analyses. For tissue imaging, images were acquired on a Zeiss LSM 880 with Airyscan
428 using a Plan-Apochromat 63x/1.4 NA oil DIC M27 and 1.8x zoom. Images were Airyscan
429 processed prior to analysis. Threshold, laser power, and gain were kept constant for each
430 experiment. Z-stacks of identical size were taken at similar depths were maximum projected.

431 **Image analysis**

432 Analyses of imaging data were performed using FIJI (ImageJ). For particle detection and tracking
433 we used the ImageJ plugin TrackMate³⁴. We used the Laplacian of Gaussian filter for detection
434 where the [estimated blob diameter] was set to 5 pixels and [threshold] at 30. These values were
435 determined empirically by evaluating several randomly selected reference images of GFP-FMRP
436 and comparing the contrast values of all particles detected: $[(\text{intensity inside} - \text{intensity outside}) /$
437 $(\text{intensity inside} + \text{intensity outside})]^{34}$. We tested a range of blob diameters from 3 to 6 pixel at
438 one pixel intervals. Range of threshold values were tested from 15 to 50 at intervals of 5. From
439 these conditions, we selected blob diameter and threshold values that yielded fewest particles
440 with negative contrast values (where outside is brighter than inside of the puncta) while limiting
441 detection of large spurious structures. We also used [median filter] and [sub-pixel localization] for
442 improved gaussian fit and x-y localization of fluorescent puncta. These conditions were applied
443 identically to all images to maintain consistency in the analysis. For analysis of Halo-FMRP and
444 Halo-S499A, we used similar conditions for puncta analysis, except contrast since tissue
445 generally resulted in variable background from slice to slice. To normalize, we used SNR (signal
446 to noise) calculation in TrackMate: $[(\text{intensity inside} - \text{intensity outside}) / \text{standard deviation of the}$
447 $\text{puncta intensity}]^{34}$. Statistical comparisons were made using unpaired, two-tailed student's t-test
448 or Mann-Whitney test in Prism.

449 For tracking granules, we used the default settings for the [Simple LAP] tracker with [maximum
450 linking distance] of 5 pixels and [maximum gap-closing distance] of 5 pixels. In most situations

451 puncta density did not result in overlapping particles. As such, we used the same value as our
452 blob diameter as the upper-limit for non-diffusive motion. The [maximum gap-closing frame gap]
453 was set to 2. To select for processively moving particles, we first identified all particle trajectories
454 using TrackMate and sorted for processivity using our MATLAB script (available on github.com).
455 In brief, each trajectory of a particle was rotated based on its longest axis of movement, which is
456 the direction of processive movement. Once rotated, 5 or more consecutive positive or negative
457 displacements in the long axis was defined as the processive movement. Kymographs of
458 trafficking puncta were generated using the ImageJ plugin Kymographbuilder.

459 For single particle tracking, the [estimated blob diameter] was set to 5 pixels and [threshold] at
460 30. Under high illumination, single JFX dye molecules produce a point spread function that fits a
461 gaussian profile within the 5-pixel diameter. Next, we used the [Simple LAP] tracker with
462 [maximum linking distance] of 15 pixels and [maximum gap-closing distance] of 15 pixels, as the
463 molecules were sparsely populated in the dendrites. The [maximum gap-closing frame gap] was
464 set to 2. We used less stringent criteria to accommodate particles that were more confined in
465 Halo-FMRP, relative to Halo-I304N particles that were more freely moving. In addition, we
466 selected tracks with 5 or more continuously tracked frames to remove spurious detection of fast-
467 moving dyes and shot noise from the detector.

468 For FRAP analysis, we selected a 9-pixel circular region of interest (ROI) around the bleach
469 puncta and measured average intensity within the ROI for all timepoints. The average intensity
470 values were normalized to pre image ($t = -30$ s) and the error bars denote standard deviation (SD).
471 Background fluorescence was measured from a 14x14 area at least 100 pixels away from the site
472 of photobleaching that did not contain any cellular fluorescence from all timepoints. The average
473 background fluorescence was subtracted from the average fluorescence from the bleached ROI
474 at each timepoint. To compare between drug treated and untreated FRAP experiments with
475 different photobleaching efficiency, the first timepoint after photobleaching was set to baseline
476 (zero) and all subsequent recovery values were baseline subtracted. The fluorescence recovery
477 values were fit to a nonlinear regression curve (one-phase association) using Prism to derive time
478 constants (τ) or time at half-maximal fluorescence of the recovery. The normalized fluorescence
479 recovery at the final timepoint were analyzed using unpaired, two-tailed student's t-test.

480 **Statistical analyses**

481 In all results where statistical information was included, at least three or more independent trials
482 were performed. Statistical comparisons were made using unpaired student's t-test where p-

483 values and sample sizes (n) were included in the Figure Legend. Standard deviation (SD) values
484 were reported for photobleaching results and all others show standard error of the mean (SEM).

485 **Figure legend**

486 **Figure 1. FXS patient-derived I304N FMRP does not stably bind FMRP granules. a.**

487 Representative fluorescence image (pseudo-colored as inverted grayscale) of a dendrite
488 expressing the I304N mutant FMRP for one week. Scale bar is 5 μm . **b.** Comparison of
489 kymographs from GFP-FMRP (left) or GFP-I304N (right) expressing dendrites. The discrete
490 stationary fluorescent puncta present in GFP-FMRP are depicted as continuous lines along the
491 time-axis while the I304N dendrite does not exhibit any stationary particles. **c.** Sparse labeled
492 HaloTag-FMRP (Halo-FMRP, pink circles) overlaid with particle trajectories that are color-coded
493 by total displacement. LUT denotes total displacement during 5 second imaging epoch ranging
494 from 0 to 3.9 μm . Scale bar is 5 μm . See also Supplemental Movie 1. **d.** Sparse labeled HaloTag-
495 I304N FMRP (Halo-I304N, pink circles) overlaid with particle trajectories that are color-coded by
496 total displacement. See also Supplemental Movie 1. LUT denotes total displacement during 5
497 second imaging epoch ranging from 0 to 4.0 μm . **e.** Scatter plot of total displacement by Halo-
498 FMRP (black circles; $n=359$ tracks from 11 cells) and Halo-I304N (red circles; $n=299$ tracks from
499 11 cells) particles. The horizontal lines denote population median. Statistical significance was
500 tested using unpaired, two-tailed Mann-Whitney test. $p^{****} < 0.0001$. **f.** Scatter plot of mean
501 velocity of Halo-FMRP (black circles) and Halo-I304N (red circles) particles. Statistical
502 significance was tested using unpaired, two-tailed Mann-Whitney test. $p^{****} < 0.0001$. **g.** Scatter
503 plot of mean particle diameter per dendrite of Halo-FMRP ($n=11$) and Halo-I304N particles ($n=11$).
504 The horizontal lines denote population mean. Statistical significance was tested using unpaired,
505 two-tailed t-test. ns, not significant. **h.** Scatter plot of mean particle intensity per dendrite of Halo-
506 FMRP and Halo-I304N particles. The horizontal lines denote population mean. Statistical
507 significance was tested using unpaired, two-tailed t-test. ns, not significant.

508 **Figure 2. S499 phospho-mutant FMRP form distinct granules. a.** Schematic of fluorescent

509 FMRP reporter constructs: human Synapsin promoter drives the expression of GFP-FMRP. Red
510 lines denote location of I304 and S499. **b.** Cartoon of FMRP reporter in green binding to FMRP
511 granules. Over time, fluorescent FMRP exchanges with endogenous FMRP which allows
512 granules to become fluorescent. **c.** A 10x magnification view of cultured neurons expressing GFP-
513 FMRP labeled with antibodies to GFP shown in green. DAPI is shown in blue. Scale bar is 50 μm .
514 **d.** A representative dendrite expressing GFP-FMRP (top panel, inverted grayscale). Same
515 dendrite shown in 16-color LUT (middle panel). Overlay with TrackMate particle detection (pink
516 circles, bottom panel). Scale bar is 5 μm . **e.** Surface plot of FMRP puncta shown in the dotted box
517 in (d). Numbers on surface plot correspond to puncta in inset. The LUT indicates the minimum

518 and maximum fluorescence intensity range. **f.** Violin plots of granule diameter from GFP-FMRP
519 (green; n=32; 10905 granules), S499A (magenta; n=36; 4923 granules) and S499D (blue; n=14;
520 3088 granules). Horizontal lines denote population median. Statistical significance was calculated
521 using unpaired, two-tailed student's t-test. $p^{****} < 0.0001$. **g.** Violin plots of granule fluorescence
522 intensity from GFP-FMRP (green; n=32), S499A (magenta; n=36) and S499D (blue; n=14).
523 Horizontal lines denote population median. Statistical significance was calculated using unpaired,
524 two-tailed student's t-test. $p^{**} < 0.01$; $p^{****} < 0.0001$. **h.** Violin plots of granule contrast from GFP-
525 FMRP (green; n=32), S499A (magenta; n=36) and S499D (blue; n=14). Horizontal lines denote
526 population median. Statistical significance was calculated using unpaired, two-tailed student's t-
527 test. $p^{**} < 0.01$.

528 **Figure 3. FMRP phospho-mutant granules differ in processive movement.** **a.** Fluorescence
529 images of GFP-FMRP (top), S499A (middle) and S499D (bottom) expressing dendrites overlaid
530 with tracks detected by TrackMate. LUT indicates velocity at $\mu\text{m}/\text{sec}$ and the scale bar is $5 \mu\text{m}$.
531 See also Supplemental Movie 2-4. **b.** Histogram of $\log_{10}(\text{Displacement})$ of GFP-FMRP (top,
532 green), S499A (middle, magenta), and S499D (bottom, blue) granules where displacement is
533 calculated as the distance from the beginning and end of processive movement in microns.
534 Histograms were normalized by the total counts in the population. Dotted lines indicate two peaks
535 from distributions. For GFP-FMRP, $P_{\langle \text{high displacement} \rangle} = 0.366$ and $P_{\langle \text{low displacement} \rangle} = 0.634$;
536 $\text{Displacement}_{\text{high}} = 0.58 \mu\text{m}$ and $\text{Displacement}_{\text{low}} = 0.09 \mu\text{m}$. For S499A, $P_{\langle \text{high displacement} \rangle} = 0.30$
537 and $P_{\langle \text{low displacement} \rangle} = 0.70$; $\text{Displacement}_{\text{high}} = 0.45 \mu\text{m}$ and $\text{Displacement}_{\text{low}} = 0.09 \mu\text{m}$. For S499D,
538 $P_{\langle \text{high displacement} \rangle} = 0.436$ and $P_{\langle \text{low displacement} \rangle} = 0.564$; $\text{Displacement}_{\text{high}} = 0.64 \mu\text{m}$ and
539 $\text{Displacement}_{\text{low}} = 0.14 \mu\text{m}$.

540 **Figure 4. FMRP granules exchange FMRP proteins in a translation-dependent manner.** **a.**
541 Schematic of spot photobleaching of individual FMRP granules. **b.** Representative image of GFP-
542 FMRP granule (green) in dendritic segment (red) selected for the fluorescence recovery assay.
543 The white arrowhead indicates the photobleached granule and the scale bar is $5 \mu\text{m}$. See also
544 Supplemental Movie 5. **c.** Time-series montage of FMRP granule recovery. Time is noted on the
545 top-right in seconds. **d.** Representative image of GFP-FMRP granule (green) FRAP in the
546 presence of cycloheximide (CHX). The white arrowhead indicates the photobleached granule and
547 the scale bar is $5 \mu\text{m}$. See also Supplemental Movie 7. **e.** Time-series montage of FMRP granule
548 recovery in CHX. **f.** Plot of normalized average fluorescence recovery \pm SD (shaded bars) for
549 granules expressing GFP-FMRP (black circles; n=12) and CHX-treatment (red circles; n=12) over

550 time. The recovery values were fit to a nonlinear regression curve (gray dashed lines) to calculate
551 time constants (τ). The dotted line indicates the average baseline intensity following
552 photobleaching set to zero. **g.** Normalized recovery at the final timepoint for GFP-FMRP (black
553 circles; n=12) and CHX-treatment (red circles; n=12). Horizontal lines denote population mean.
554 Statistical significance was calculated using unpaired, two-tailed student's t-test. $p^{****} < 0.0001$.
555 **h.** Normalized recovery \pm SD for S499A granules (black circles; n=10) and CHX-treatment (red
556 circles; n=11). **i.** Normalized recovery at the final timepoint for S499A (black circles; n=10) and
557 CHX-treatment (red circles; n=11). Statistical significance was calculated using unpaired, two-
558 tailed student's t-test. $p^{****} < 0.0001$. **j.** Normalized recovery \pm SD for S499D granules (black
559 circles; n=8) and CHX-treatment (red circles; n=12). **k.** Normalized recovery at the final timepoint
560 for S499D (black circles; n=8) and CHX-treatment (red circles; n=12). Statistical significance was
561 calculated using unpaired, two-tailed student's t-test. ns, not significant. **l.** Model of how
562 phosphorylation changes FMRP granule dimensions, translation and transport. Dotted circle
563 indicates FMRP granule formed by predominantly phosphorylated (left) or dephosphorylated
564 (right) FMRP. The bidirectional arrow indicates the change in the phospho-state of FMRP. Circled
565 P indicates phosphate groups. Green up-arrow indicates increase and red down-arrow indicates
566 decrease.

567 **Figure 5. Halo-S499A FMRP leads to increased protein synthesis in mossy fiber boutons.**

568 **a.** Representative tiled fluorescence image of a hippocampal slice expressing Halo-FMRP labeled
569 with JF549 HaloTag ligand after targeted stereotactic injection into the dentate gyrus (DG). Mossy
570 fiber projections (MFs) containing boutons from Halo-FMRP-expressing neurons are shown in the
571 white box. **b-c.** Representative images of mossy fiber boutons expressing Halo-FMRP or Halo-
572 S499A. Scale bar is 10 μ m. Insets show higher magnification of boutons **d.** Violin plot of Halo-
573 FMRP (black; n=3650 boutons) and Halo-S499A (red; n=2556 boutons) granule diameters.
574 Horizontal lines denote population median. Statistical significance was calculated using unpaired,
575 two-tailed student's t-test. $p^{****} < 0.0001$. **e.** Scatter plot of Halo-FMRP (black; n=3650) and Halo-
576 S499A (red; n=2556) granule intensities. Horizontal lines denote population median. Statistical
577 significance was calculated using unpaired, two-tailed student's t-test. $p^{****} < 0.0001$. **f.** Violin plot
578 of Halo-FMRP (black; n=3650) and Halo-S499A (red; n=2556) granule signal-to-noise ratio (SNR).
579 Horizontal lines denote population median. Statistical significance was calculated using unpaired,
580 two-tailed student's t-test. $p^{****} < 0.0001$. **g-h.** Representative images of puromycin labeling (PMY,
581 green) and JF549 HaloTag labeling (red) in slices from mice injected with Halo-FMRP (left) or
582 Halo-S499A (right). The FMRP fluorescence was used as a mask to measure puromycin signal.

583 Scale bar is 10 μm . Insets show higher magnification of boutons. **i.** The average intensity of
584 colocalized puromycin label in Halo-FMRP (n=6 slices) and Halo-S499A (n=6 slices) were
585 normalized to Halo-FMRP. Statistical significance was calculated using unpaired, two-tailed
586 student's t-test. $p^{****} < 0.001$.

587 **References**

- 588 1 Bagni, C. & Zukin, R. S. A Synaptic Perspective of Fragile X Syndrome and Autism
589 Spectrum Disorders. *Neuron* **101**, 1070-1088, doi:10.1016/j.neuron.2019.02.041 (2019).
- 590 2 Richter, J. D., Bassell, G. J. & Klann, E. Dysregulation and restoration of translational
591 homeostasis in fragile X syndrome. *Nat Rev Neurosci* **16**, 595-605, doi:10.1038/nrn4001
592 (2015).
- 593 3 Darnell, J. C. & Klann, E. The translation of translational control by FMRP: therapeutic
594 targets for FXS. *Nat Neurosci* **16**, 1530-1536, doi:10.1038/nn.3379 (2013).
- 595 4 Hagerman, R. J. *et al.* Fragile X syndrome. *Nat Rev Dis Primers* **3**, 17065,
596 doi:10.1038/nrdp.2017.65 (2017).
- 597 5 Qin, M., Kang, J., Burlin, T. V., Jiang, C. & Smith, C. B. Postadolescent changes in
598 regional cerebral protein synthesis: an in vivo study in the FMR1 null mouse. *J Neurosci*
599 **25**, 5087-5095, doi:10.1523/JNEUROSCI.0093-05.2005 (2005).
- 600 6 Huber, K. M., Gallagher, S. M., Warren, S. T. & Bear, M. F. Altered synaptic plasticity in
601 a mouse model of fragile X mental retardation. *Proc Natl Acad Sci U S A* **99**, 7746-7750,
602 doi:10.1073/pnas.122205699 (2002).
- 603 7 Stefani, G., Fraser, C. E., Darnell, J. C. & Darnell, R. B. Fragile X mental retardation
604 protein is associated with translating polyribosomes in neuronal cells. *J Neurosci* **24**,
605 7272-7276, doi:10.1523/JNEUROSCI.2306-04.2004 (2004).
- 606 8 Khandjian, E. W. *et al.* Biochemical evidence for the association of fragile X mental
607 retardation protein with brain polyribosomal ribonucleoparticles. *Proc Natl Acad Sci U S*
608 *A* **101**, 13357-13362, doi:10.1073/pnas.0405398101 (2004).
- 609 9 Brown, V. *et al.* Microarray identification of FMRP-associated brain mRNAs and altered
610 mRNA translational profiles in fragile X syndrome. *Cell* **107**, 477-487,
611 doi:10.1016/s0092-8674(01)00568-2 (2001).
- 612 10 Darnell, J. C. *et al.* FMRP stalls ribosomal translocation on mRNAs linked to synaptic
613 function and autism. *Cell* **146**, 247-261, doi:10.1016/j.cell.2011.06.013 (2011).
- 614 11 Antar, L. N., Afroz, R., Dichtenberg, J. B., Carroll, R. C. & Bassell, G. J. Metabotropic
615 glutamate receptor activation regulates fragile x mental retardation protein and FMR1
616 mRNA localization differentially in dendrites and at synapses. *J Neurosci* **24**, 2648-2655,
617 doi:10.1523/JNEUROSCI.0099-04.2004 (2004).
- 618 12 Dichtenberg, J. B., Swanger, S. A., Antar, L. N., Singer, R. H. & Bassell, G. J. A direct role
619 for FMRP in activity-dependent dendritic mRNA transport links filopodial-spine
620 morphogenesis to fragile X syndrome. *Dev Cell* **14**, 926-939,
621 doi:10.1016/j.devcel.2008.04.003 (2008).
- 622 13 Napoli, I. *et al.* The fragile X syndrome protein represses activity-dependent translation
623 through CYFIP1, a new 4E-BP. *Cell* **134**, 1042-1054, doi:10.1016/j.cell.2008.07.031
624 (2008).
- 625 14 Muddashetty, R. S. *et al.* Reversible inhibition of PSD-95 mRNA translation by miR-
626 125a, FMRP phosphorylation, and mGluR signaling. *Mol Cell* **42**, 673-688,
627 doi:10.1016/j.molcel.2011.05.006 (2011).
- 628 15 Ceman, S. *et al.* Phosphorylation influences the translation state of FMRP-associated
629 polyribosomes. *Hum Mol Genet* **12**, 3295-3305, doi:10.1093/hmg/ddg350 (2003).
- 630 16 Narayanan, U. *et al.* FMRP phosphorylation reveals an immediate-early signaling
631 pathway triggered by group I mGluR and mediated by PP2A. *J Neurosci* **27**, 14349-
632 14357, doi:10.1523/JNEUROSCI.2969-07.2007 (2007).
- 633 17 Niere, F., Wilkerson, J. R. & Huber, K. M. Evidence for a fragile X mental retardation
634 protein-mediated translational switch in metabotropic glutamate receptor-triggered Arc
635 translation and long-term depression. *J Neurosci* **32**, 5924-5936,
636 doi:10.1523/JNEUROSCI.4650-11.2012 (2012).

- 637 18 Nalavadi, V. C., Muddashetty, R. S., Gross, C. & Bassell, G. J. Dephosphorylation-
638 induced ubiquitination and degradation of FMRP in dendrites: a role in immediate early
639 mGluR-stimulated translation. *J Neurosci* **32**, 2582-2587,
640 doi:10.1523/JNEUROSCI.5057-11.2012 (2012).
- 641 19 Monday, H. R., Kharod, S. C., Yoon, Y. J., Singer, R. H. & Castillo, P. E. Presynaptic
642 FMRP and local protein synthesis support structural and functional plasticity of
643 glutamatergic axon terminals. *Neuron* **110**, 2588-2606 e2586,
644 doi:10.1016/j.neuron.2022.05.024 (2022).
- 645 20 Estes, P. S., O'Shea, M., Clasen, S. & Zarnescu, D. C. Fragile X protein controls the
646 efficacy of mRNA transport in Drosophila neurons. *Mol Cell Neurosci* **39**, 170-179,
647 doi:10.1016/j.mcn.2008.06.012 (2008).
- 648 21 El Fatimy, R. *et al.* Tracking the Fragile X Mental Retardation Protein in a Highly
649 Ordered Neuronal RiboNucleoParticles Population: A Link between Stalled
650 Polyribosomes and RNA Granules. *PLoS Genet* **12**, e1006192,
651 doi:10.1371/journal.pgen.1006192 (2016).
- 652 22 Christie, S. B., Akins, M. R., Schwob, J. E. & Fallon, J. R. The FXG: a presynaptic fragile
653 X granule expressed in a subset of developing brain circuits. *J Neurosci* **29**, 1514-1524,
654 doi:10.1523/JNEUROSCI.3937-08.2009 (2009).
- 655 23 Lai, A., Valdez-Sinon, A. N. & Bassell, G. J. Regulation of RNA granules by FMRP and
656 implications for neurological diseases. *Traffic* **21**, 454-462, doi:10.1111/tra.12733 (2020).
- 657 24 Adinolfi, S. *et al.* The N-terminus of the fragile X mental retardation protein contains a
658 novel domain involved in dimerization and RNA binding. *Biochemistry* **42**, 10437-10444,
659 doi:10.1021/bi034909g (2003).
- 660 25 Zhang, Y. *et al.* The fragile X mental retardation syndrome protein interacts with novel
661 homologs FXR1 and FXR2. *EMBO J* **14**, 5358-5366, doi:10.1002/j.1460-
662 2075.1995.tb00220.x (1995).
- 663 26 De Boule, K. *et al.* A point mutation in the FMR-1 gene associated with fragile X mental
664 retardation. *Nat Genet* **3**, 31-35, doi:10.1038/ng0193-31 (1993).
- 665 27 Feng, Y. *et al.* FMRP associates with polyribosomes as an mRNP, and the I304N
666 mutation of severe fragile X syndrome abolishes this association. *Mol Cell* **1**, 109-118,
667 doi:10.1016/s1097-2765(00)80012-x (1997).
- 668 28 Zang, J. B. *et al.* A mouse model of the human Fragile X syndrome I304N mutation.
669 *PLoS Genet* **5**, e1000758, doi:10.1371/journal.pgen.1000758 (2009).
- 670 29 Grimm, J. B. *et al.* A general method to improve fluorophores for live-cell and single-
671 molecule microscopy. *Nat Methods* **12**, 244-250, 243 p following 250,
672 doi:10.1038/nmeth.3256 (2015).
- 673 30 Grimm, J. B. *et al.* A General Method to Improve Fluorophores Using Deuterated
674 Auxochromes. *JACS Au* **1**, 690-696, doi:10.1021/jacsau.1c00006 (2021).
- 675 31 Bartley, C. M. *et al.* Mammalian FMRP S499 Is Phosphorylated by CK2 and Promotes
676 Secondary Phosphorylation of FMRP. *eNeuro* **3**, doi:10.1523/ENEURO.0092-16.2016
677 (2016).
- 678 32 Formicola, N., Vijayakumar, J. & Besse, F. Neuronal ribonucleoprotein granules:
679 Dynamic sensors of localized signals. *Traffic* **20**, 639-649, doi:10.1111/tra.12672 (2019).
- 680 33 Arsenault, J. *et al.* FMRP Expression Levels in Mouse Central Nervous System Neurons
681 Determine Behavioral Phenotype. *Hum Gene Ther* **27**, 982-996,
682 doi:10.1089/hum.2016.090 (2016).
- 683 34 Tinevez, J. Y. *et al.* TrackMate: An open and extensible platform for single-particle
684 tracking. *Methods* **115**, 80-90, doi:10.1016/j.ymeth.2016.09.016 (2017).
- 685 35 Linghu, C. *et al.* Spatial Multiplexing of Fluorescent Reporters for Imaging Signaling
686 Network Dynamics. *Cell* **183**, 1682-1698 e1624, doi:10.1016/j.cell.2020.10.035 (2020).

- 687 36 Antar, L. N., Dichtenberg, J. B., Plociniak, M., Afroz, R. & Bassell, G. J. Localization of
688 FMRP-associated mRNA granules and requirement of microtubules for activity-
689 dependent trafficking in hippocampal neurons. *Genes Brain Behav* **4**, 350-359,
690 doi:10.1111/j.1601-183X.2005.00128.x (2005).
- 691 37 Antar, L. N., Li, C., Zhang, H., Carroll, R. C. & Bassell, G. J. Local functions for FMRP in
692 axon growth cone motility and activity-dependent regulation of filopodia and spine
693 synapses. *Mol Cell Neurosci* **32**, 37-48, doi:10.1016/j.mcn.2006.02.001 (2006).
- 694 38 Wilbertz, J. H. *et al.* Single-Molecule Imaging of mRNA Localization and Regulation
695 during the Integrated Stress Response. *Mol Cell* **73**, 946-958 e947,
696 doi:10.1016/j.molcel.2018.12.006 (2019).
- 697 39 Liao, Y. C. *et al.* RNA Granules Hitchhike on Lysosomes for Long-Distance Transport,
698 Using Annexin A11 as a Molecular Tether. *Cell* **179**, 147-164 e120,
699 doi:10.1016/j.cell.2019.08.050 (2019).
- 700 40 Tsang, B. *et al.* Phosphoregulated FMRP phase separation models activity-dependent
701 translation through bidirectional control of mRNA granule formation. *Proc Natl Acad Sci*
702 *U S A* **116**, 4218-4227, doi:10.1073/pnas.1814385116 (2019).
- 703 41 Riback, J. A. *et al.* Composition-dependent thermodynamics of intracellular phase
704 separation. *Nature* **581**, 209-214, doi:10.1038/s41586-020-2256-2 (2020).
- 705 42 Yang, P. *et al.* G3BP1 Is a Tunable Switch that Triggers Phase Separation to Assemble
706 Stress Granules. *Cell* **181**, 325-345 e328, doi:10.1016/j.cell.2020.03.046 (2020).
- 707 43 Kim, T. H. *et al.* Phospho-dependent phase separation of FMRP and CAPRIN1
708 recapitulates regulation of translation and deadenylation. *Science* **365**, 825-829,
709 doi:10.1126/science.aax4240 (2019).
- 710 44 Birsa, N. *et al.* FUS-ALS mutants alter FMRP phase separation equilibrium and impair
711 protein translation. *Sci Adv* **7**, doi:10.1126/sciadv.abf8660 (2021).
- 712 45 Kharod, S. C., Monday, H. R., Yoon, Y. J. & Castillo, P. E. Protocol to study presynaptic
713 protein synthesis in ex vivo mouse hippocampal slices using HaloTag technology. *STAR*
714 *Protoc* **4**, 101986, doi:10.1016/j.xpro.2022.101986 (2023).
- 715 46 Schmidt, E. K., Clavarino, G., Ceppi, M. & Pierre, P. SUnSET, a nonradioactive method
716 to monitor protein synthesis. *Nat Methods* **6**, 275-277, doi:10.1038/nmeth.1314 (2009).
- 717 47 Wu, B., Eliscovich, C., Yoon, Y. J. & Singer, R. H. Translation dynamics of single
718 mRNAs in live cells and neurons. *Science* **352**, 1430-1435, doi:10.1126/science.aaf1084
719 (2016).
- 720 48 Shu, H. *et al.* FMRP links optimal codons to mRNA stability in neurons. *Proc Natl Acad*
721 *Sci U S A* **117**, 30400-30411, doi:10.1073/pnas.2009161117 (2020).
- 722 49 Doma, M. K. & Parker, R. Endonucleolytic cleavage of eukaryotic mRNAs with stalls in
723 translation elongation. *Nature* **440**, 561-564, doi:10.1038/nature04530 (2006).
- 724 50 Chen, E., Sharma, M. R., Shi, X., Agrawal, R. K. & Joseph, S. Fragile X mental
725 retardation protein regulates translation by binding directly to the ribosome. *Mol Cell* **54**,
726 407-417, doi:10.1016/j.molcel.2014.03.023 (2014).
- 727 51 Myasnikov, A. G. *et al.* Structure-function insights reveal the human ribosome as a
728 cancer target for antibiotics. *Nat Commun* **7**, 12856, doi:10.1038/ncomms12856 (2016).
- 729 52 Shen, L. *et al.* Structure of the translating *Neurospora* ribosome arrested by
730 cycloheximide. *Proc Natl Acad Sci U S A* **118**, doi:10.1073/pnas.2111862118 (2021).
- 731 53 Goering, R. *et al.* FMRP promotes RNA localization to neuronal projections through
732 interactions between its RGG domain and G-quadruplex RNA sequences. *Elife* **9**,
733 doi:10.7554/eLife.52621 (2020).
- 734 54 Kurosaki, T. *et al.* Loss of the fragile X syndrome protein FMRP results in misregulation
735 of nonsense-mediated mRNA decay. *Nat Cell Biol* **23**, 40-48, doi:10.1038/s41556-020-
736 00618-1 (2021).

737 55 Zhang, G. *et al.* Dynamic FMR1 granule phase switch instructed by m6A modification
738 contributes to maternal RNA decay. *Nat Commun* **13**, 859, doi:10.1038/s41467-022-
739 28547-7 (2022).
740 56 Yoon, Y. J. *et al.* Glutamate-induced RNA localization and translation in neurons. *Proc*
741 *Natl Acad Sci U S A* **113**, E6877-E6886, doi:10.1073/pnas.1614267113 (2016).
742
743

744 **Acknowledgements**

745 We would like to thank Dr. Hannah Monday for comments and reading of the manuscript. We
746 also thank the Singer lab and Castillo lab members for their comments and discussions. We are
747 grateful to the Lavis lab and HHMI/Janelia Research Campus for the JF dyes. We are also
748 grateful to Stephanie Ceman and Jeff Chao for providing plasmids on Addgene. This research
749 was supported by the National Institutes of Health: R01-MH125772, R01-NS113600, R01-
750 NS115543, R01-MH116673 to P.E.C; R01-NS083085 to R.H.S.; shared instrument grant
751 (S10OD025295) to Kostantin Dobrenis; R21-MH120496 to Y.J.Y.

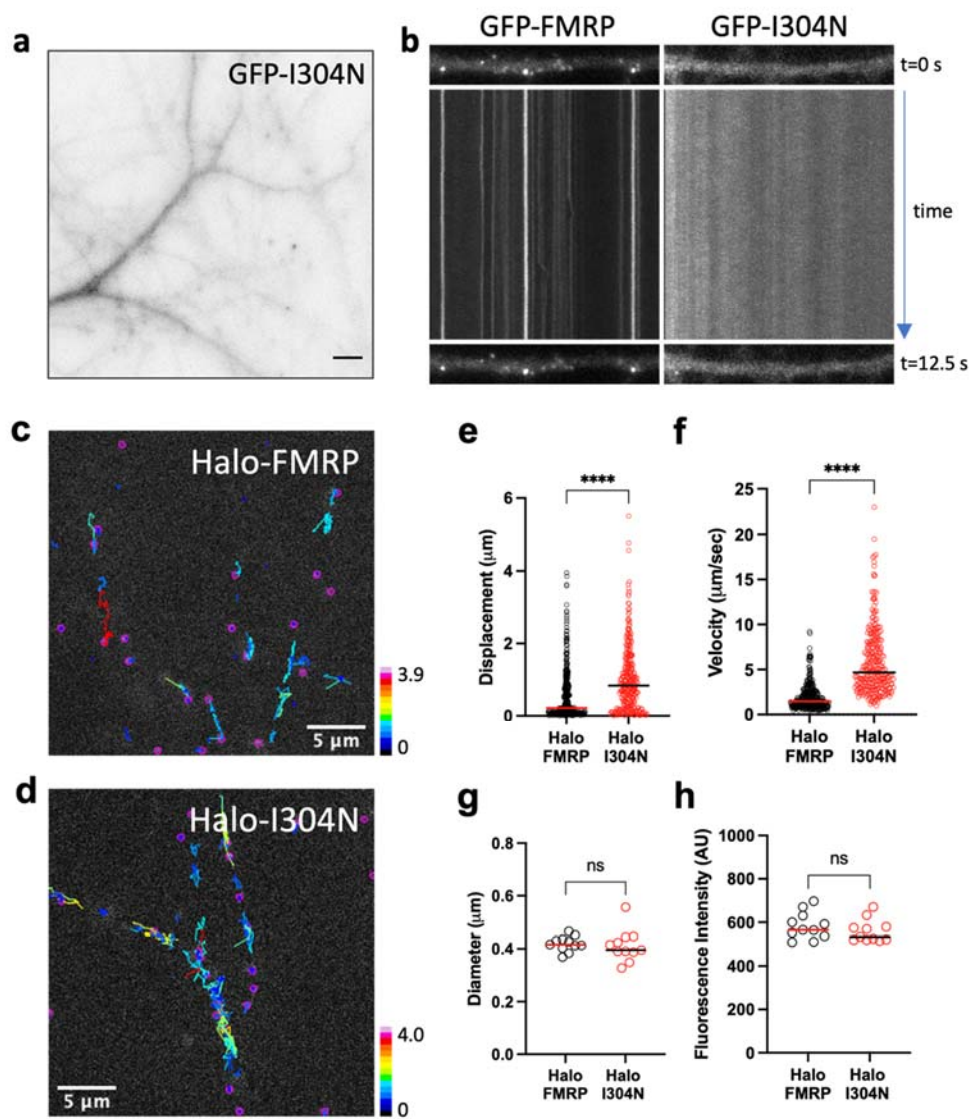
752 **Author contributions**

753 S.C.K., P.E.C, R.H.S. and Y.J.Y designed the research. S.C.K., D.H. and Y.J.Y. performed the
754 experiments and analyses. H.C. performed particle processivity analysis. K.J.Y. performed
755 single-molecule tracking analysis. S.C.K. and Y.J.Y. wrote the paper and was edited by P.E.C.,
756 R.H.S. and Y.J.Y.

757 **Competing interests**

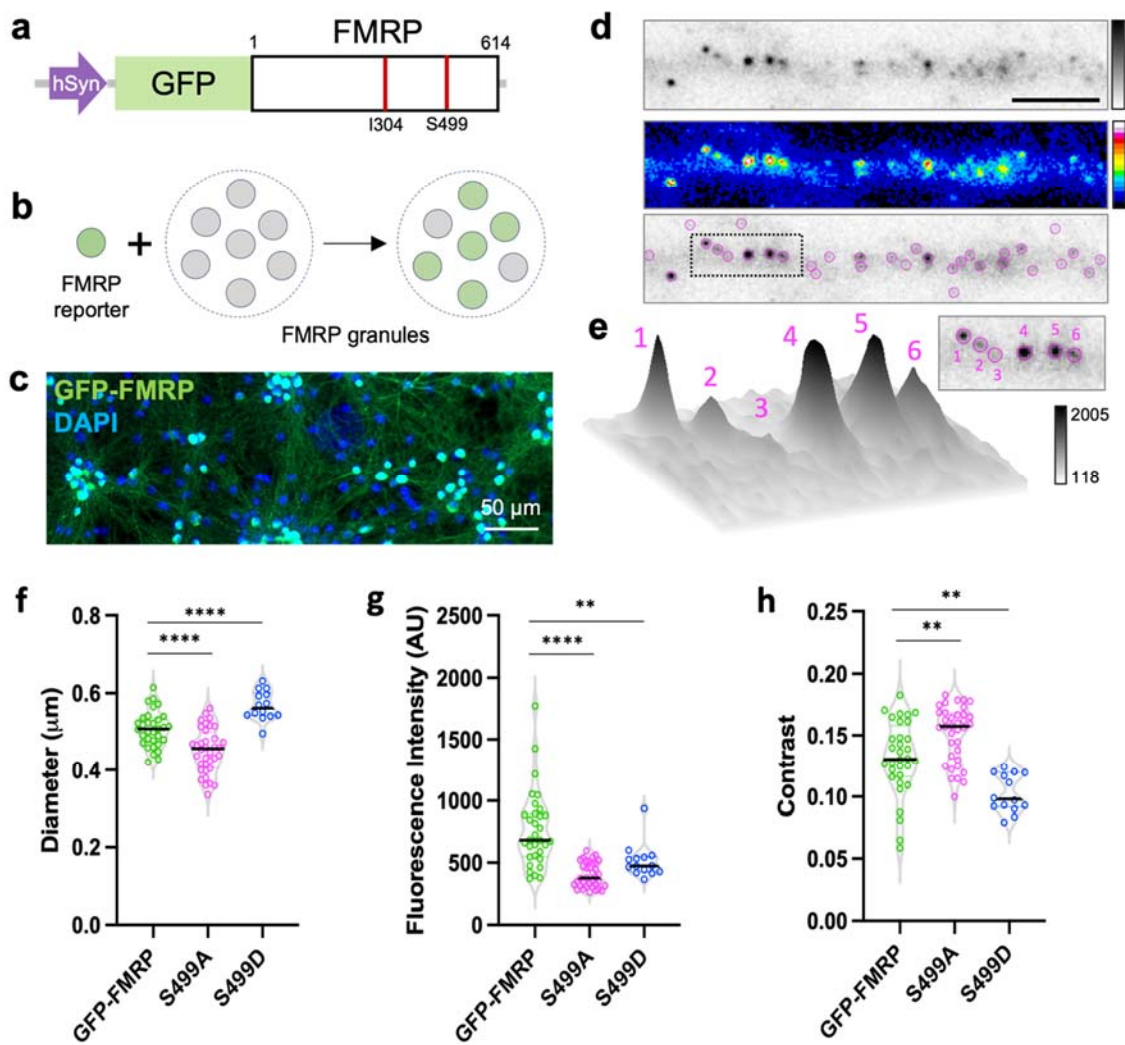
758 The authors declare no competing interests.
759

Figure 1



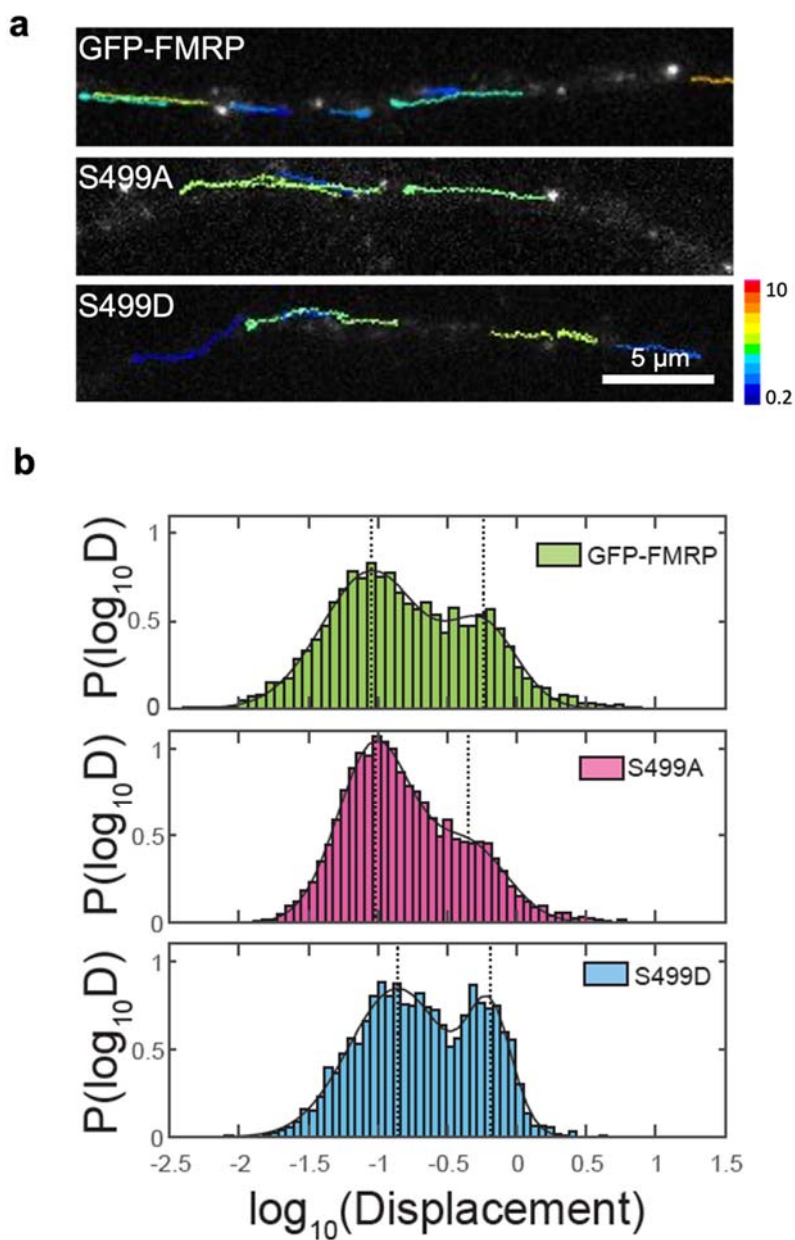
760

Figure 2



761

Figure 3



762

Figure 4

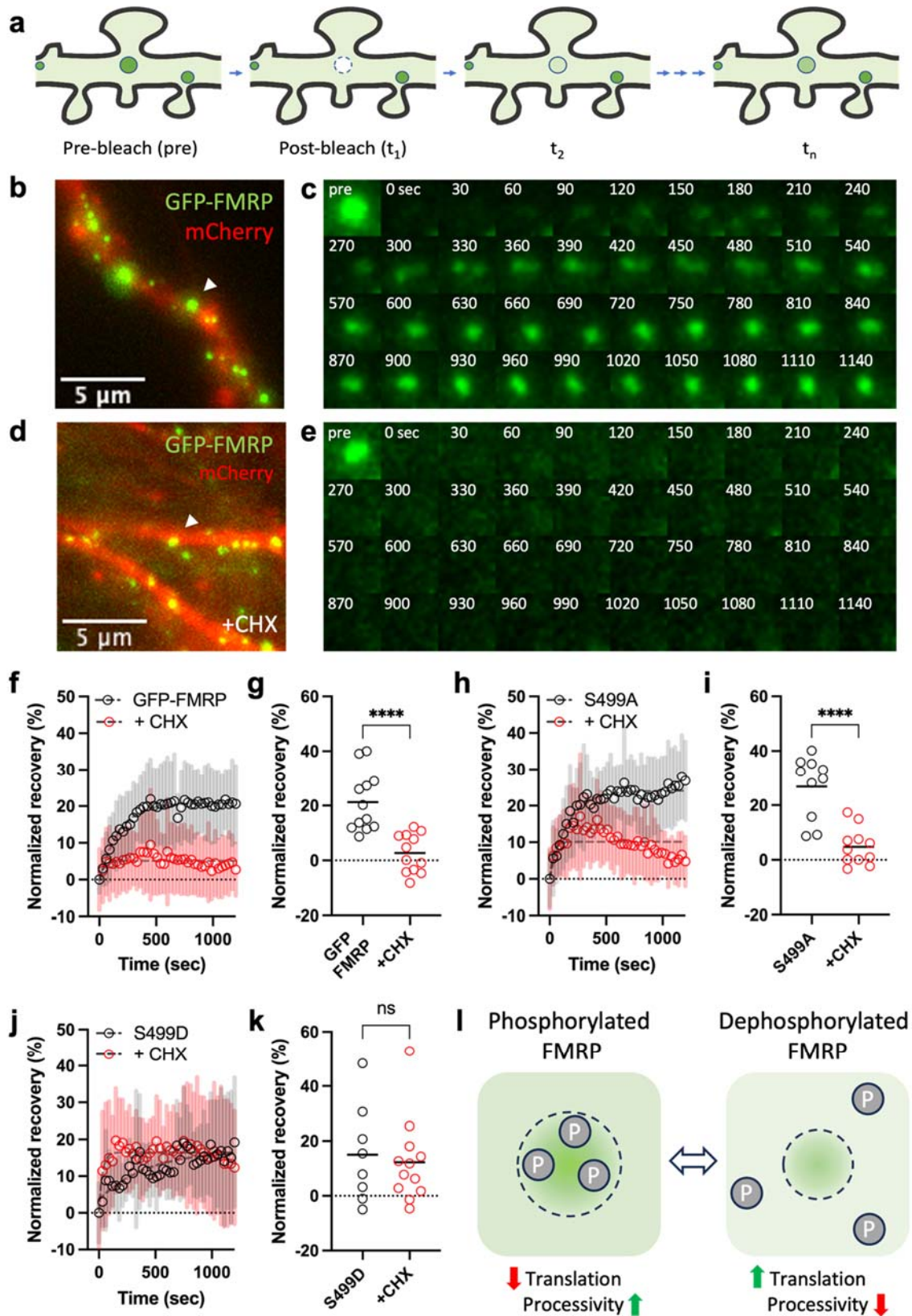
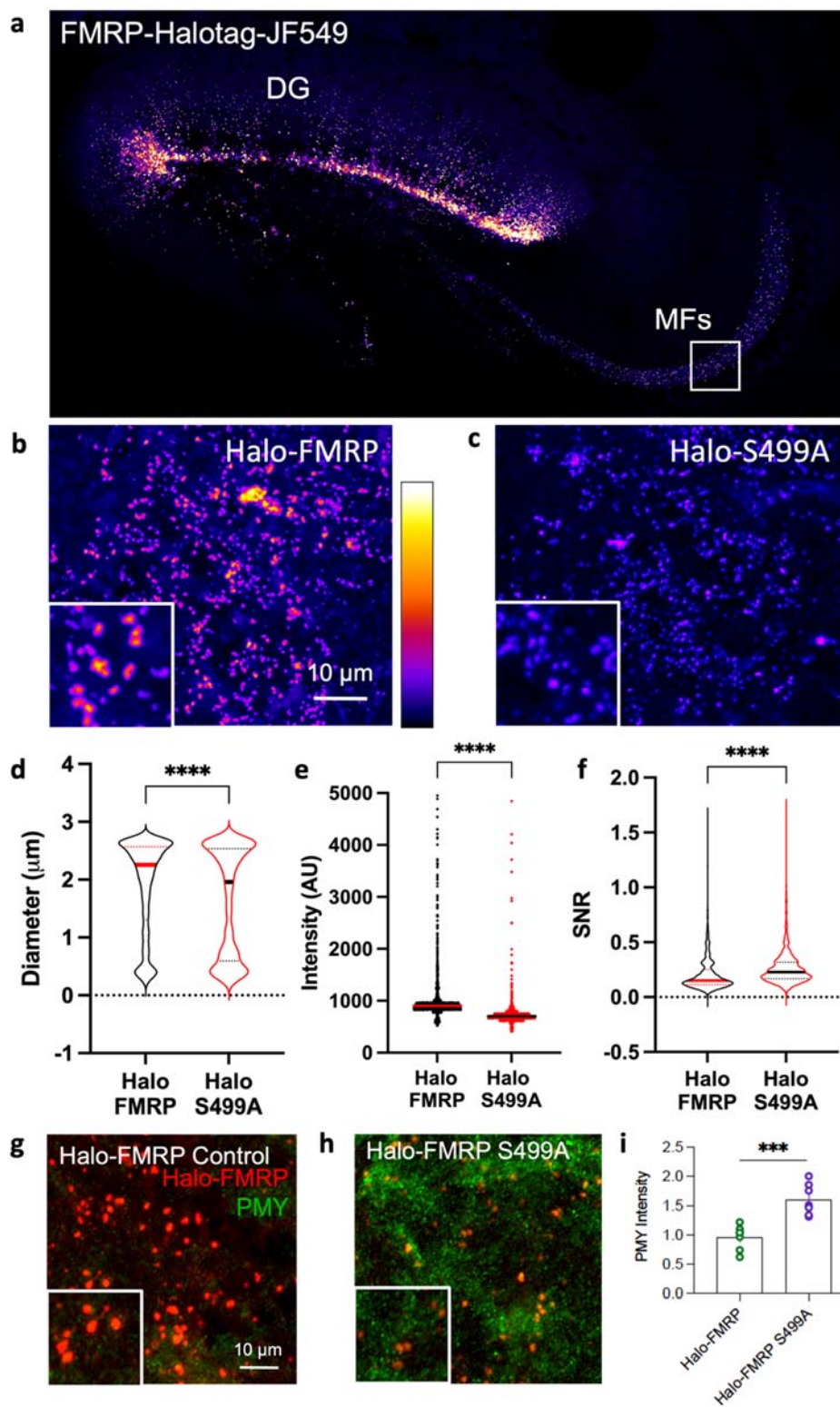


Figure 5



1
2
3
4
5
6
7
8
9
10
11
12
13
14
15
16
17
18
19
20
21
22

Supplementary Information

Phosphorylation alters FMRP granules and determines their transport or protein synthesis abilities

Shivani C. Kharod¹, Dongwoo Hwang², Heejun Choi⁴, Kyle J. Yoon², Pablo E. Castillo^{1,3} Robert H. Singer^{1,2} and Young J. Yoon^{1,2,*}

¹ *Dominick P. Purpura Department of Neuroscience, Albert Einstein College of Medicine, NY 10461*

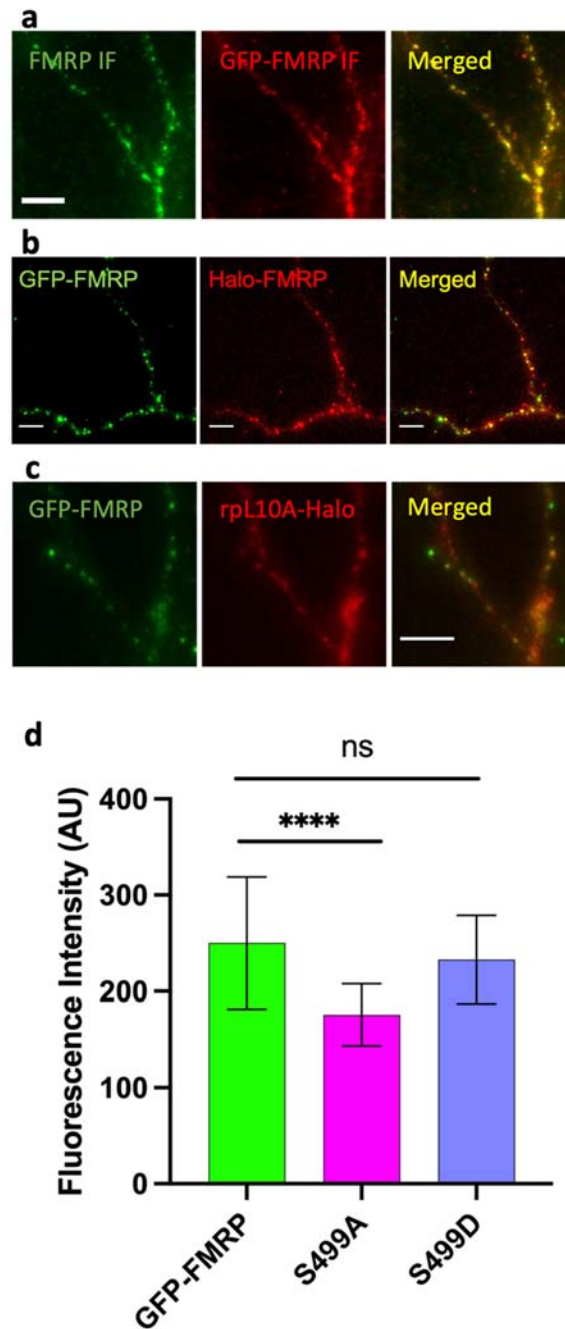
² *Department of Cell Biology, Albert Einstein College of Medicine, NY 10461*

³ *Department of Psychiatry and Behavioral Sciences, Albert Einstein College of Medicine, NY 10461*

⁴ *Janelia Research Campus, HHMI, Ashburn, VA 20147*

Supplementary Figures 1-6
Supplementary Movies 1-14

Supplemental figure 1

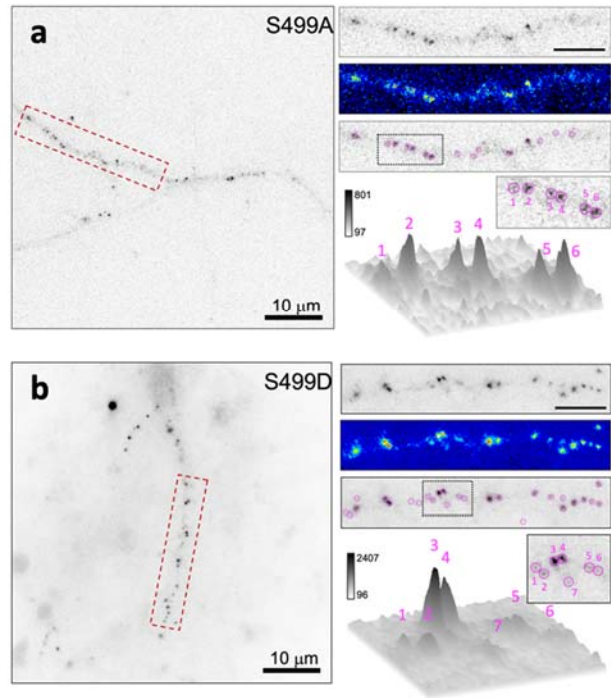


23
24

25 **Figure S1. FMRP reporters colocalize with endogenous FMRP and Halotagged ribosomal**
26 **protein L10A. a.** Immunofluorescence using antibodies to FMRP (Abcam; ab17722) shown in
27 green and GFP (Aves lab) in red and merged image on the right. Cultured hippocampal neurons
28 were infected with lentivirus encoding GFP-FMRP at DIV7, antibody labeled and imaged at DIV14.
29 High degree of colocalization can be observed. Scale bar is 5 μ m. **b.** Live image of dendrites
30 expressing both GFP-FMRP (green) and Halo-FMRP (red) labeled with JF646, along with the
31 merged image on the right. Both reporters were expressed in neurons at DIV7 and imaged at
32 DIV14. Many granules exhibit discrete colocalization of both reporters. Scale bar is 5 μ m. **c.** Live

33 image of dendrites expressing GFP-FMRP (green) and ribosomal protein L10A-Halo (red) labeled
34 with JF646, along with the merged image on the right. Many granules exhibit colocalization of
35 reporter proteins. Both reporters were expressed in neurons at DIV7 and imaged at DIV14. Scale
36 bar is 5 μ m. **d.** Average fluorescence intensities from dendrites expression GFP-FMRP (green),
37 S499A (magenta) and S499D (blue). Statistical significance was calculated using unpaired, two-
38 tailed student's t-test. $p^{****} < 0.0001$.

Supplemental figure 2

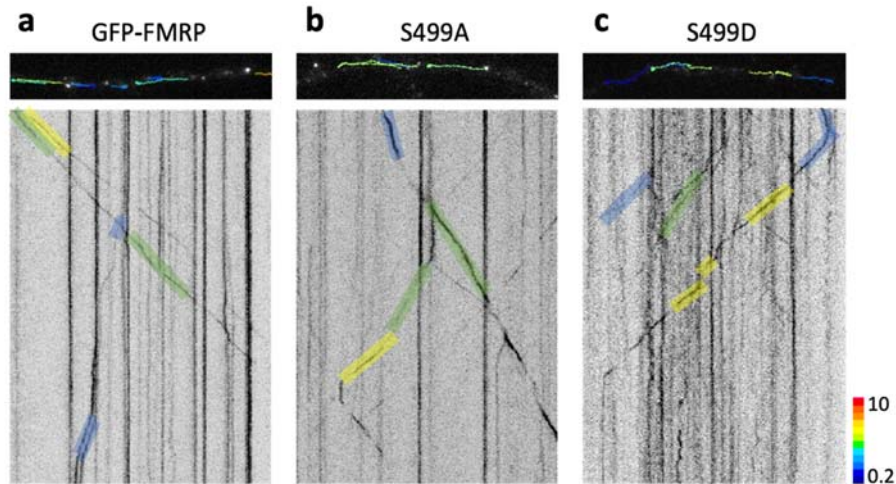


39
40

41 **Figure S2. S499 mutant FMRP reporters differ in their binding to FMRP granules. a.**
42 Representative dendrite expressing the GFP-S499A reporter (inverted grayscale). A dendritic
43 segment is outlined in the dashed box. Scale bar is 10 µm. Top right panel shows the enlarged
44 dendrite in the dashed box. Scale bar is 5 µm. Middle right panel shows the same dendrite in 16-
45 color LUT. Bottom panel shows the dendrite overlaid with TrackMate particle detection (pink
46 circles). Below the panels is a surface plot of S499A puncta shown in the dotted box. Numbers
47 on surface plot correspond to puncta in inset. The LUT indicates the minimum and maximum
48 fluorescence intensity range. **b.** Representative dendrite expressing the GFP-S499D reporter
49 (inverted grayscale). A dendritic segment is outlined in the dashed box. Scale bar is 10 µm. Top
50 right panel shows the enlarged dendrite in the dashed box. Scale bar is 5 µm. Middle right panel
51 shows the same dendrite in 16-color LUT. Bottom panel shows the dendrite overlaid with
52 TrackMate particle detection (pink circles). Below the panels is a surface plot of S499A puncta
53 shown in the dotted box. Numbers on surface plot correspond to puncta in inset. The LUT
54 indicates the minimum and maximum fluorescence intensity range.

55

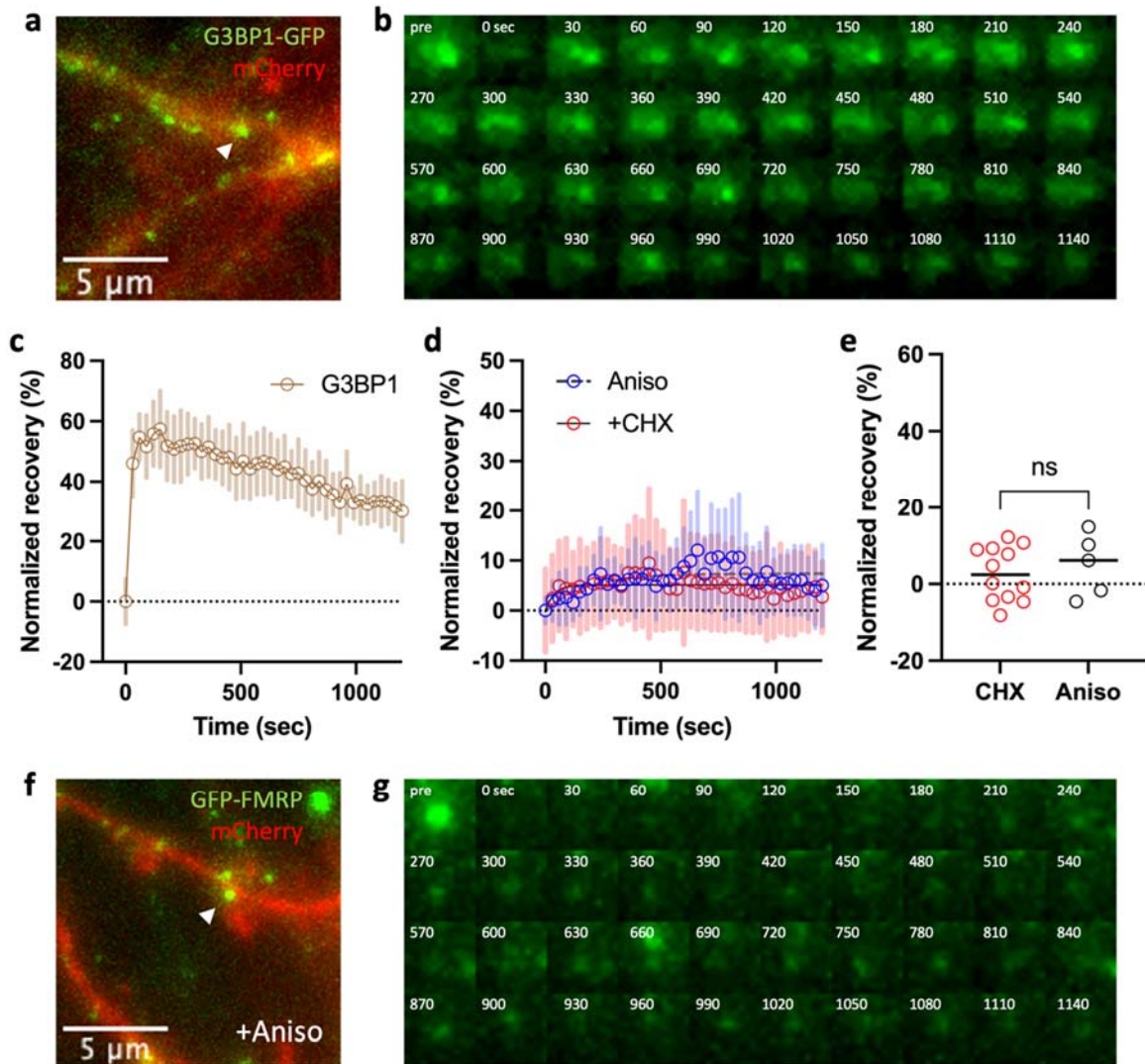
Supplemental figure 3



56
57

58 **Figure S3. FMRP reporter containing granules move along dendrites.** a. Representative
59 fluorescence image of GFP-FMRP dendrites overlaid with tracks detected by TrackMate.
60 Dendrites were imaged at 50 ms per frame for 400 consecutive frames (20 seconds total; see
61 also Supplemental Movies 2-4). The streaming movies were converted to LUT-inverted
62 kymograph to visualize moving particles along the x-t axis. Horizontal lines indicate non-moving
63 particles and diagonal lines indicate moving particles where the slope indicate the speed (i.e.
64 steeper slope is slower and flatter slope is faster). The tracks were overlaid with color-coded
65 shades to indicate average speed of granule. b. Fluorescence image of GFP-S499A dendrite and
66 kymograph. c. Fluorescence image of GFP-S499D dendrite and kymograph. LUT indicates
67 average velocity of granules ranging from 0.2 to 10 $\mu\text{m}/\text{sec}$.

Supplemental figure 4

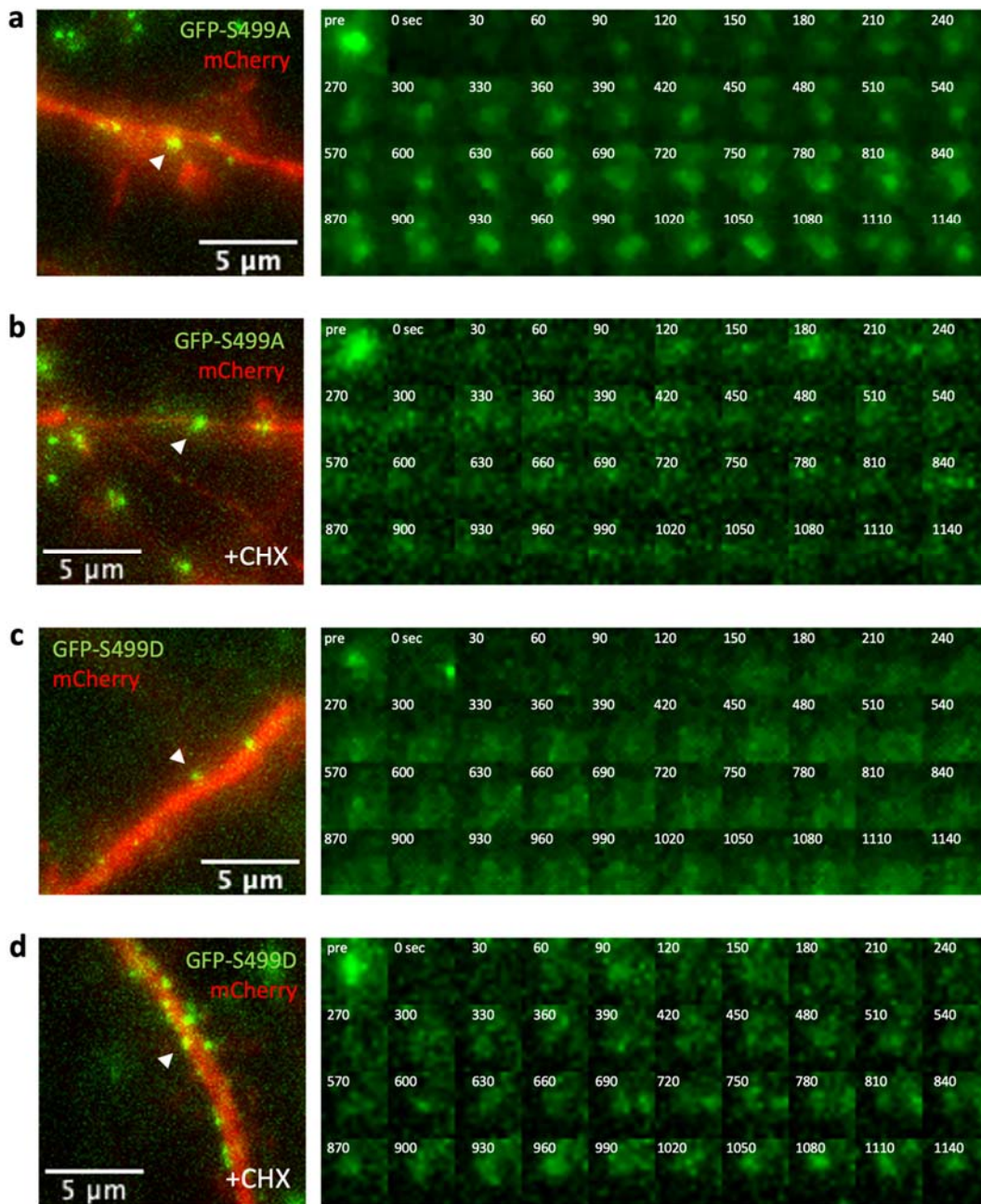


68
69

70 **Figure S4. FMRP granule recovery after photobleaching is different compared to G3BP1**
 71 **and is sensitive to anisomycin.** **a.** Representative image of G3BP1-GFP granule (green) in
 72 dendritic segment (red) selected for FRAP assay. White arrowhead indicates the photobleached
 73 granule and the scale bar is 5 μm . See also Supplemental Movie 6. **b.** Time-series montage of
 74 G3BP1-GFP granule recovery. Time is noted on the top-right in seconds. **c.** Plot of normalized
 75 average fluorescence recovery \pm SD (shaded bars) for G3BP1-GFP granules (brown circles; $n=9$)
 76 over time. The dotted line indicates the average baseline intensity following photobleaching set
 77 to zero. **d.** Plot of normalized average fluorescence recovery \pm SD (shaded bars) for granules
 78 expressing GFP-FMRP under cycloheximide-treatment (CHX, red circles; $n=12$) or anisomycin-
 79 treatment (Aniso, blue circles; $n=5$) over time. The recovery values were fit to a nonlinear
 80 regression curve (gray dashed lines) to calculate time constants (τ). The dotted line indicates the
 81 average baseline intensity following photobleaching set to zero. **e.** Plot of normalized recovery at
 82 the final the timepoint for CHX-treatment (red circles; $n=12$) and Aniso-treatment (blue circles;
 83 $n=5$). The dotted line indicates the average baseline intensity following photobleaching set to zero.

84 Horizontal lines denote population median. Statistical significance was calculated using unpaired,
85 two-tailed student's t-test. ns, not significant. **f.** Representative image of GFP-FMRP granule
86 (green) in dendritic segment (red) selected for FRAP assay in the presence of anisomycin
87 (+Aniso). White arrowhead indicates the photobleached granule and the scale bar is 5 μm . See
88 also Supplemental Movie 8. **g.** Time-series montage of GFP-FMRP granule recovery in the
89 presence of anisomycin. Time is noted on the top-right in seconds.

Supplemental figure 5

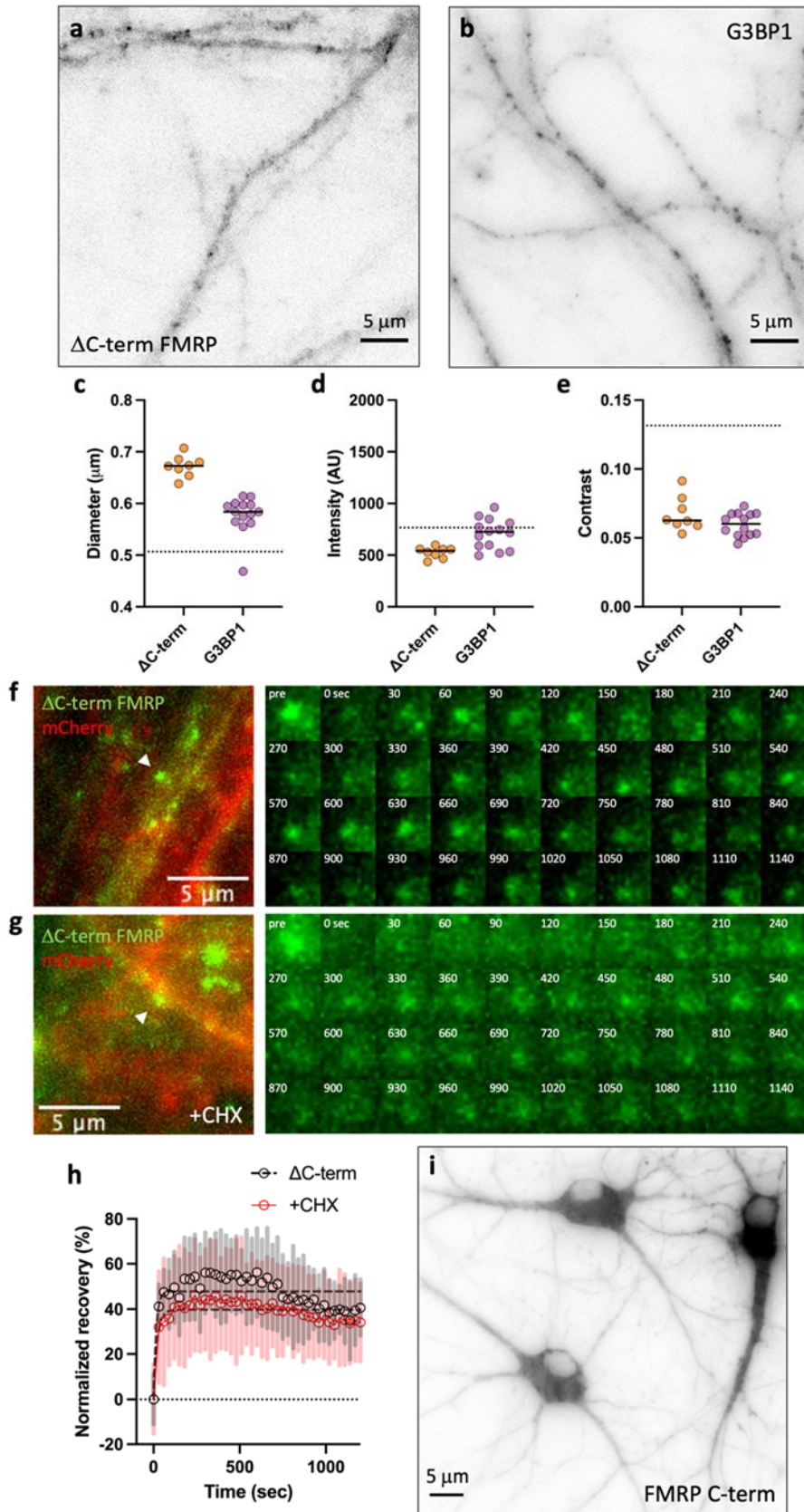


90
91

92 **Figure S5. FMRP phospho-mutant granule recovery after photobleaching differ between**
93 **S499A and S499D mutants.** **a.** Representative image of GFP-S499A granule (green) in dendritic
94 segment (red) selected for FRAP assay. White arrowhead indicates the photobleached granule
95 and the scale bar is 5 μm. See also Supplemental Movie 9. On the right is a time-series montage
96 of GFP-S499A granule recovery. Time is noted on the top-right in seconds. **b.** Representative
97 image of GFP-S499A granule (green) in dendritic segment (red) selected for FRAP assay in the
98 presence of cycloheximide (+CHX). White arrowhead indicates the photobleached granule and

99 the scale bar is 5 μm . See also Supplemental Movie 10. On the right is a time-series montage of
100 GFP-S499A granule recovery. Time is noted on the top-right in seconds. **c.** Representative image
101 of GFP-S499D granule (green) in dendritic segment (red) selected for FRAP assay. White
102 arrowhead indicates the photobleached granule and the scale bar is 5 μm . See also Supplemental
103 Movie 11. On the right is a time-series montage of GFP-S499D granule recovery. Time is noted
104 on the top-right in seconds. **d.** Representative image of GFP-S499D granule (green) in dendritic
105 segment (red) selected for FRAP assay in the presence of cycloheximide (+CHX). White
106 arrowhead indicates the photobleached granule and the scale bar is 5 μm . See also Supplemental
107 Movie 12. On the right is a time-series montage of GFP-S499D granule recovery. Time is noted
108 on the top-right in seconds.

Supplemental figure 6



110 **Figure S6. S499 is necessary but not sufficient for granule binding.** **a.** Representative
111 fluorescence image (pseudo-colored as inverted grayscale) of a dendrite expressing the mutant
112 FMRP reporter that does not have the C-terminal region (Δ C-term). Scale bar is 5 μ m. **b.**
113 Representative image of G3BP1-GFP granules in dendrites. Scale bar is 5 μ m. **c.** Scatter plot of
114 average diameter of fluorescent granules in neurons expressing Δ C-term FMRP (orange; n=8;
115 2768 granules) or G3BP1 (purple; n=14; 3422 granules). Horizontal lines denote population
116 median. Dashed line indicates median GFP-FMRP granule diameter (0.507 μ m). **d.** Scatter plot
117 of average intensity of fluorescent granules in neurons expressing Δ C-term FMRP (orange; n=8)
118 or G3BP1 (purple; n=14). Horizontal lines denote population median. Dashed line indicates
119 median GFP-FMRP granule intensity (765.3 AU). **e.** Scatter plot of average contrast of fluorescent
120 granules in neurons expressing Δ C-term FMRP (orange; n=8) or G3BP1 (purple; n=14).
121 Horizontal lines denote population median. Dashed line indicates median GFP-FMRP granule
122 contrast (0.132). **f.** Representative image of Δ C-term FMRP granule (green) in dendritic segment
123 (red) selected for FRAP assay. White arrowhead indicates the photobleached granule and the
124 scale bar is 5 μ m. See also Supplemental Movie 13. On the right is a time-series montage of Δ C-
125 term FMRP granule recovery. Time is noted on the top-right in seconds. **g.** Representative image
126 of Δ C-term FMRP granule (green) in dendritic segment (red) selected for FRAP assay in the
127 presence of cycloheximide (+CHX). White arrowhead indicates the photobleached granule and
128 the scale bar is 5 μ m. See also Supplemental Movie 14. On the right is a time-series montage of
129 Δ C-term FMRP granule recovery. Time is noted on the top-right in seconds. **h.** Plot of normalized
130 average fluorescence recovery \pm SD (shaded bars) for Δ C-term FMRP granules (black circles;
131 n=8) and cycloheximide-treatment (CHX, red circles; n=8) over time. The recovery values were
132 fit to a nonlinear regression curve (gray dashed lines) to calculate time constants (τ). The dotted
133 line indicates the average baseline intensity following photobleaching set to zero. **i.**
134 Representative fluorescence image (pseudo-colored as inverted grayscale) of cultured neurons
135 expressing the FMRP C-terminal region (FMRP C-term). Scale bar is 5 μ m.

136 **Supplementary Movie 1. Movie of single particle tracking of Halo-FMRP and Halo-I304N.**

137 On the top-left is the Halo-FMRP raw images and on the top-right is the Halo-FMRP particles
138 detected by TrackMate (pink circles) overlaid with trajectories color-coded by total displacement.
139 On the bottom-left is the Halo-I304N raw images and on the bottom-right is the Halo-FMRP
140 particles detected by TrackMate (pink circles) overlaid with trajectories color-coded by total
141 displacement. The movie is running at 50 frames per second.

142 **Supplementary Movie 2. Movie of GFP-FMRP granules in dendrites overlaid with tracks.**

143 On the left is a dendrite expressing GFP-FMRP and on the right is the same dendrite overlaid
144 with particle tracks detected by TrackMate color-coded by displacement. The movie is running at
145 50 frames per second.

146 **Supplementary Movie 3. Movie of GFP-S499A granules in dendrites overlaid with tracks.**

147 On the left is a dendrite expressing GFP-S499A and on the right is the same dendrite overlaid
148 with particle tracks detected by TrackMate color-coded by displacement. The movie is running at
149 50 frames per second.

150 **Supplementary Movie 4. Movie of GFP-S499D granules in dendrites overlaid with tracks.**

151 On the left is a dendrite expressing GFP-S499D and on the right is the same dendrite overlaid
152 with particle tracks detected by TrackMate color-coded by displacement. The movie is running at
153 50 frames per second.

154 **Supplementary Movie 5. Movie of GFP-FMRP granule recovery after photobleaching.**

155 On the left is a dendrite expressing GFP-FMRP and mCherry where the photobleached granule is
156 circled. Shown on the right is GFP-FMRP only. The movie is running at 15 frames per second.

157 **Supplementary Movie 6. Movie of G3BP1-GFP granule recovery after photobleaching.**

158 On the left is a dendrite expressing G3BP1-GFP and mCherry where the photobleached granule is
159 circled. Shown on the right is G3BP1-GFP only. The movie is running at 15 frames per second.

160 **Supplementary Movie 7. Movie of GFP-FMRP granule recovery after photobleaching in**

161 **cycloheximide.** On the left is a dendrite expressing GFP-FMRP and mCherry where the
162 photobleached granule is circled. Shown on the right is GFP-FMRP only. The movie is running at
163 15 frames per second.

164 **Supplementary Movie 8. Movie of GFP-FMRP granule recovery after photobleaching in**

165 **anisomycin.** On the left is a dendrite expressing GFP-FMRP and mCherry where the
166 photobleached granule is circled. Shown on the right is GFP-FMRP only. The movie is running at
167 15 frames per second.

168 **Supplementary Movie 9. Movie of GFP-S499A granule recovery after photobleaching.**

169 On the left is a dendrite expressing GFP-S499A and mCherry where the photobleached granule is
170 circled. Shown on the right is GFP-S499A only. The movie is running at 15 frames per second.

171 **Supplementary Movie 10. Movie of GFP-S499A granule recovery after photobleaching in**

172 **cycloheximide.** On the left is a dendrite expressing GFP-S499A and mCherry where the
173 photobleached granule is circled. Shown on the right is GFP-S499A only. The movie is running
174 at 15 frames per second.

175 **Supplementary Movie 11. Movie of GFP-S499D granule recovery after photobleaching.** On
176 the left is a dendrite expressing GFP-S499D and mCherry where the photobleached granule is
177 circled. Shown on the right is GFP-S499D only. The movie is running at 15 frames per second.

178 **Supplementary Movie 12. Movie of GFP-S499D granule recovery after photobleaching in**
179 **cycloheximide.** On the left is a dendrite expressing GFP-S499D and mCherry where the
180 photobleached granule is circled. Shown on the right is GFP-S499D only. The movie is running
181 at 15 frames per second.

182 **Supplementary Movie 13. Movie of Δ C-term FMRP granule recovery after photobleaching.**
183 On the left is a dendrite expressing Δ C-term FMRP and mCherry where the photobleached
184 granule is circled. Shown on the right is Δ C-term FMRP only. The movie is running at 15 frames
185 per second.

186 **Supplementary Movie 14. Movie of Δ C-term FMRP granule recovery after photobleaching**
187 **in cycloheximide.** On the left is a dendrite expressing Δ C-term FMRP and mCherry where the
188 photobleached granule is circled. Shown on the right is Δ C-term FMRP only. The movie is running
189 at 15 frames per second.